

Linear and Nonlinear Optical Responses in Kitaev Spin Liquids

Minoru Kanega,^{1,*} Tatsuhiko N. Ikeda,^{2,†} and Masahiro Sato^{1,‡}

¹*Department of Physics, Ibaraki University, Mito, Ibaraki 310-8512, Japan*

²*Institute for Solid State Physics, University of Tokyo, Kashiwa, Chiba 277-8581, Japan*

(Dated: July 30, 2021)

We theoretically study THz-light-driven high-harmonic generation (HHG) in the spin-liquid states of the Kitaev honeycomb model with a magnetostriction coupling between spin and electric polarization. To compute the HHG spectra, we numerically solve the Lindblad equation, taking account of the dissipation effect. We find that isotropic Kitaev models possess a dynamical symmetry, which is broken by a static electric field, analogous to HHG in electron systems. We show that the HHG spectra exhibit characteristic continua of Majorana fermion excitations, and their broad peaks can be controlled by applying static electric or magnetic fields. In particular, the magnetic-field dependence of the HHG spectra drastically differs from those of usual ordered magnets. These results indicate that an intense THz laser provides a powerful tool to observe dynamic features of quantum spin liquids.

Introduction.— Quantum spin liquids (QSLs) have attracted tremendous attention for decades as exotic states of matter. Many theoreticians have tried to find essential properties of QSLs, and it has been theoretically revealed that the low-energy excitations of QSLs are given by fractionalized particles and the wave functions possess a topological nature [1–4].

Meanwhile, it has been recognized as notoriously difficult to identify QSLs experimentally because most of their thermodynamic quantities are featureless. Hence, the experiments have been done for their dynamical quantities. For instance, longitudinal [5–7] and transverse [8, 9] transport phenomena have provided important information about low-energy excitations in QSLs. For the Kitaev QSL [10–14], ferromagnetic α -RuCl₃ has been shown to exhibit several characteristic behaviors in, e.g., the thermal Hall effect [15], longitudinal thermal conductivity [7], and Raman scattering [16, 17], and antiferromagnetic YbCl₃ [18] has been expected to host QSL from neutron diffraction measurements. While these experimental results have been reasonably taken as evidence for QSLs, they are indirect, and active studies are ongoing to search for new ways to obtain further evidence.

One such direction is the nonlinear optical response at the THz frequency regime, which has been opened up by rapid development of THz laser technology [19–22]. Being at the energy scale of magnetic excitations, THz pulses are suitable for directly investigating and controlling quantum spin systems [23–46]. To detect crisp signatures of QSLs, the so-called THz two-dimensional coherent spectroscopy has been proposed [47] and theoretically analyzed in the Kitaev model [48]. However, in the Kitaev model, this method is based on third-order, rather than second-order, optical response and thus it requires much stronger THz pulses for successful detection. The required intensity of THz pulses can be the bottleneck in experiments since spin-light couplings are generally much weaker than

charge-light ones [37–43]. In fact, while high-harmonic generation (HHG) [49, 50] has been observed at THz frequencies in, e.g., Dirac electrons [51–53], only the second-order response has been reported [28] in magnetic insulators at present. Thus, another method based on lower-order nonlinear responses, if exists, should be useful for experimental verification of QSLs.

In this Letter, we show that a combination of an intense THz laser pulse and static electromagnetic fields uncovers characteristics of the Kitaev QSL through harmonic generation including the second-order harmonic. We numerically analyze the HHG spectra of the Kitaev model with magnetostriction-type magnetoelectric (ME) coupling [54] with the quantum master equation approach [41, 46, 55, 56] to take account of dissipation effects. In addition to broad and continuous response functions characteristic of Majorana fermions, we find that static electric fields break some symmetry and activate the second-harmonic generation (SHG), and a static magnetic field causes an anomalous shift for the harmonic spectra. These findings indicate that nonlinear response to intense THz light gives us a powerful instrument for detecting dynamical features of Kitaev QSLs. Through this study, we will build a bridge between photoscience and QSLs.

Kitaev Model and Methods.— The Hamiltonian of the Kitaev model (see Fig. 1) [58] for this work is given by

$$\hat{H}_0 = - \sum_{\alpha, \langle \mathbf{r}, \mathbf{r}' \rangle_{\alpha}} J_{\alpha} \sigma_{\mathbf{r}}^{\alpha} \sigma_{\mathbf{r}'}^{\alpha} - \kappa \sum_{\text{NNN}} \sigma_{\mathbf{r}}^x \sigma_{\mathbf{r}'}^y \sigma_{\mathbf{r}''}^z - E_{\text{dc}} \hat{P} \quad (1)$$

with

$$\hat{P} = \eta_{\text{ms}} \left(- \sum_{\langle \mathbf{r}, \mathbf{r}' \rangle_x} \sigma_{\mathbf{r}}^x \sigma_{\mathbf{r}'}^x + \sum_{\langle \mathbf{r}, \mathbf{r}' \rangle_y} \sigma_{\mathbf{r}}^y \sigma_{\mathbf{r}'}^y \right), \quad (2)$$

where $\sigma_{\mathbf{r}}^{\alpha}$ ($\alpha = x, y, z$) is the Pauli matrix on the site $\mathbf{r} = (j, k)$, and the spin-1/2 operator on \mathbf{r} is $S_{\mathbf{r}}^{\alpha} = \frac{\hbar}{2} \sigma_{\mathbf{r}}^{\alpha}$ (We set $\hbar = 1$ throughout the paper). J_{α} is the Ising

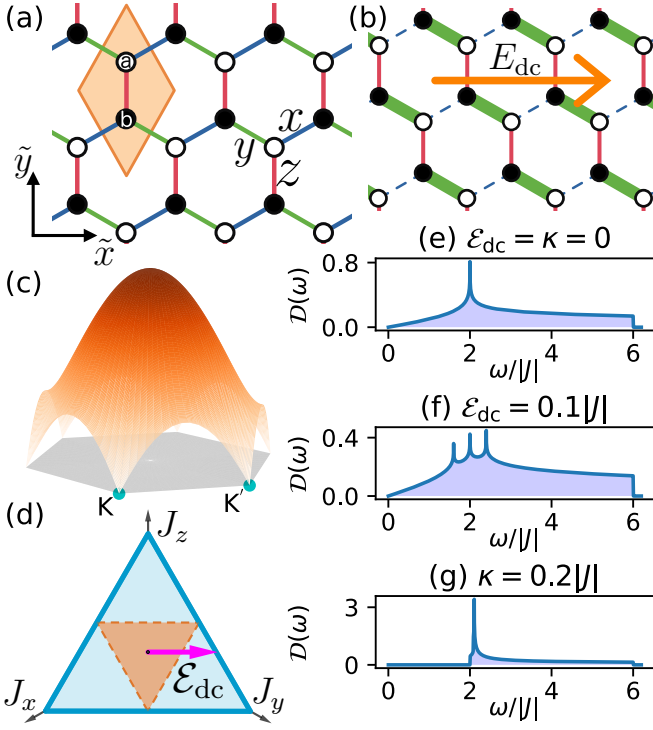


FIG. 1. (a) Lattice structure of the Kitaev model. Blue, green, and red lines respectively correspond to x , y , and z bonds. (b) Kitaev model with a dimerization on x and y bonds, which is caused by a static electric field E_{dc} along the \tilde{x} direction. (c) Gapless itinerant fermion band of the Kitaev model at $J_{x,y,z} = J$ and $E_{dc} = \kappa = 0$. (d) Ground-state phase diagram of the Kitaev model in (J_x, J_y, J_z) space at $\kappa = 0$. Orange and blue areas are respectively gapless and gapped QSLs. Application of E_{dc} induces $(J_x, J_y) \rightarrow (J_x - \mathcal{E}_{dc}, J_y + \mathcal{E}_{dc})$. (e–g) Density of states of itinerant fermions at $(\mathcal{E}_{dc}, \kappa) = (0, 0)$, $(0.1, 0)$, and $(0, 0.2)$ in $J < 0$. For detail of the density of states, see Figs. S8 and S9 of Supplemental Material [57].

coupling constant between nearest neighboring spins on α bond $\langle \mathbf{r}, \mathbf{r}' \rangle_\alpha$ and we mainly focus on the symmetric point $J = J_{x,y,z}$. The neighboring three spin term [58] originates from the third-order perturbation with respect to a static Zeeman term $\mathcal{H}_B = -g\mu_B \mathbf{B} \cdot \sum_{\mathbf{r}} \boldsymbol{\sigma}_{\mathbf{r}}^\alpha$ of an applied magnetic field \mathbf{B} (g is the g -factor and μ_B is the Bohr magneton). The coupling constant is computed as $\kappa \sim (g\mu_B)^3 B_x B_y B_z / J^2$: For $|J|/k_B = 10$ K, $\kappa \sim 0.1|J|$ corresponds to $|\mathbf{B}| \sim 1$ T. The κ term is the leading term changing the Majorana-fermion dispersion (as one will see later) in the Zeeman interaction. The final term of Eq. (1) represents the coupling between electric polarization \hat{P} and an applied static electric field E_{dc} along the \tilde{x} direction (Figs. 1(b) and 1(d)). Equation (2) assumes that \hat{P} is proportional to dimerization along the \tilde{x} direction. This kind of ME terms appears in a class of multiferroic magnets and its typical origin is the spin-phonon coupling [54]. This dimerization makes the ground-state energy reduce (see the Supplemental

Material [57]), and therefore this ME term may appear in a sort of real Kitaev-like materials. In a class of multiferroics, the ME-coupling energy reaches that of the Zeeman term [23–25, 32, 34, 54, 59, 60], and thereby we have assumed that the effective coupling $\mathcal{E}_{dc} = E_{dc}\eta_{ms}$ is the same order as $g_0\mu_B E_{dc}/c$, with c being the speed of light and $g_0 = 2$: For $|J|/k_B = 10$ K, $\mathcal{E}_{dc} \sim 0.01|J| - 0.1|J|$ corresponds to 0.1–1 MV/cm. We note that a similar dimerization ($J_x \neq J_y$) can appear in a class of Kitaev candidates even without a dc electric field.

The Kitaev model (1) is exactly solvable via fermionization [58, 61], as detailed in the literature [10–13, 58, 61] (see the Supplemental Material [57] for details). The fermionized Hamiltonian consists of four kinds of Majorana fermions: two dispersive and two localized ones (called visons). Visons have a small gap [58] and are absent [62] in the ground state at zero temperature $T = 0$. The Hamiltonian at $T = 0$ is therefore described only by the dispersive fermions. Figures 1(c)–1(g) show that the dispersive fermion is gapless around the isotropic point $J_{x,y,z} = J$, while the κ term opens a gap. We note that some perturbations can also be fermionized [63, 64], and therefore our analysis below is also applicable to such perturbed Kitaev models [65].

To consider HHG in the Kitaev model at $T = 0$, we introduce an ac ME coupling between an ac electric field $E_{ac}(t)$ and the polarization \hat{P} : $H_{ms}(t) = -E_{ac}(t)\hat{P}$ [54]. We have assumed that $\mathbf{E}_{ac} \parallel \tilde{x}$, and the field is a Gaussian pulse with a THz frequency Ω : $E_{ac}(t) = E_{ac} \cos(\Omega t) f(t)$, and the envelope function is given by $f(t) = \exp[-2(\ln 2)(t^2/t_{FWHM}^2)]$, where t_{FWHM} is the full width at half-maximum of the intensity $E_{ac}(t)^2$. We define the ac coupling constant $\mathcal{E}_{ac} = E_{ac}\eta_{ms}$ and consider five-cycle pulses ($t_{FWHM}/T = 5$). We note that even after application of $E_{ac}(t)$, the Hamiltonian $H_0 + H_{ms}(t)$ is described by a bilinear form of the dispersive fermion in wave-vector \mathbf{k} space. There is no vison dynamics in our setup that is valid in sufficiently low temperatures. We also phenomenologically introduce dissipation effects described by the Lindblad equation so as not to break the block-diagonal structure in \mathbf{k} [41, 46, 55, 56] (for details, see the Supplemental Material [57]). The dissipation is \mathbf{k} -independent and characterized by the dissipation rate $\gamma = 0.1J$, which corresponds to the relaxation time $\tau = 1/\gamma \sim 7.6$ ps for $J/k_B = 10$ K [66–75]. We suppose that the system is initially ($t \rightarrow -\infty$) in the ground state, and we solve the Lindblad equation numerically to obtain the THz-driven nonequilibrium dynamics.

The observable of interest is \hat{P} , which is the source of HHG in our model. Time evolution of polarization is given by $P(t) = \langle \hat{P} \rangle_t = N^{-1} \sum_{\mathbf{k}, k_x > 0} \text{Tr}[\rho(\mathbf{k}, t) P_{\mathbf{k}}]$, where $P_{\mathbf{k}}$ is 2×2 reduced polarization for the subspace with \mathbf{k} , and N is the total number of unit cells. Since the electromagnetic radiation is proportional to $d^2 P(t)/dt^2$,

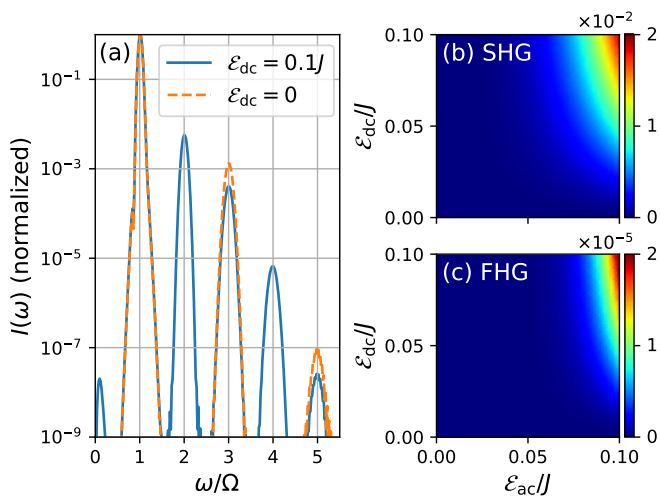


FIG. 2. HHG spectra $I(\omega)$ in driven isotropic ($J_{x,y,z} = J$) Kitaev models with/without a dc electric field E_{dc} at $\kappa = 0$ under a THz pulse of $\Omega = 2.0J$. (a) $I(\omega)$ as a function of ω at $\mathcal{E}_{dc} = 0$ and $0.1J$ under the irradiation of $\mathcal{E}_{ac} = 0.1J$. $I(\omega)$ is normalized with its maximum value. (b), (c) (E_{ac}, E_{dc}) dependence of SHG [$I(2\Omega)$] and FHG [$I(4\Omega)$] spectra. The intensities, panels (b) and (c), are normalized with $I(\Omega)$ at $\mathcal{E}_{ac} = \mathcal{E}_{dc} = 0.05J$.

the radiation power at frequency ω is given by $I(\omega) = |\omega^2 P(\omega)|^2$, where $P(\omega)$ is the Fourier transform of $P(t)$ [76]. Since a constant shift of $P(t)$ does not change $I(\omega)$, we will also use $\Delta P(t) = P(t) - P(t_{ini})$.

Effect of DC Electric Field and Dimerization.— We turn to our analyses and results. First we focus on the dc-electric-field dependence of HHG in the Kitaev model with $J_{x,y,z} = J$ and $\kappa = 0$. Figure 2(a) shows a typical HHG spectrum $I(\omega)$ for ferromagnetic ($J > 0$) Kitaev models at $\mathcal{E}_{dc} = 0$ and $0.1J$. Figures 2(b) and 2(c) are respectively the (E_{ac}, E_{dc}) dependence of the SHG and fourth harmonic generation (FHG) that arise due to dimerization by $E_{dc} \neq 0$. The SHG signal, activated by the dc electric field, is stronger than higher-order harmonics and can be a useful probe for QSL as we discuss further below.

The HHG selection rules are often understood by dynamical symmetries that become exact in the limit of $t_{FWHM} \rightarrow \infty$ [77, 78] also known as the time glide symmetry [79]. For our Kitaev model, we find that the following dynamical symmetry determines the HHG selection rule. In the non-dimerized case of $E_{dc} = 0$, the Hamiltonian $H_0 + H_{ms}(t)$ is invariant under the time translation operation $t \rightarrow t + T/2$ combined with the unitary transformation $\hat{U} = \hat{U}_{mir} \times \hat{U}_{\pi/2}^z$, where \hat{U}_{mir} is the reflection operation with respect to the \tilde{y} axis and $\hat{U}_{\pi/2}^z$ is the global $\pi/2$ spin rotation around the S^z axis. \hat{P} is odd for this transformation, and therefore we obtain $P(t+T/2) = -P(t)$, which means that even-order HHG is prohibited, consistent with Fig. 2 [57]. However,

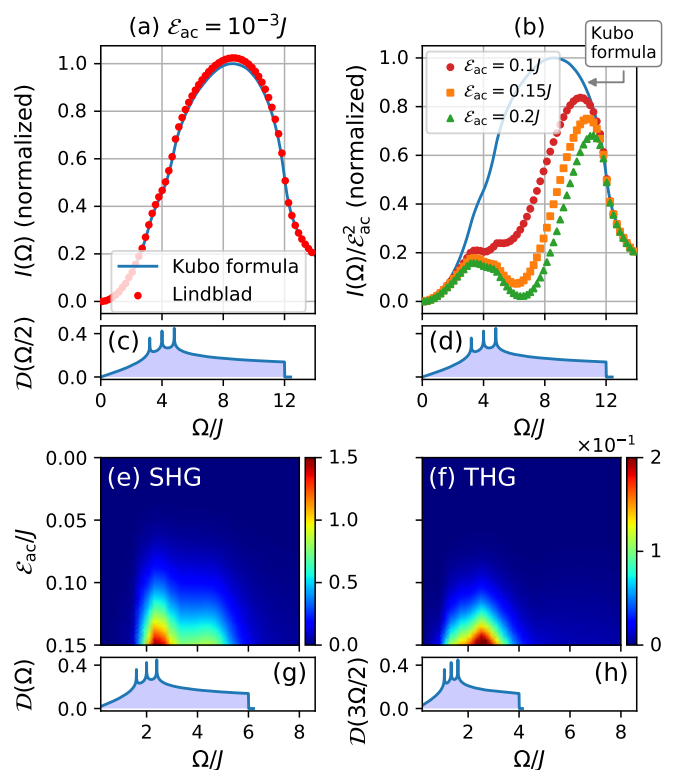


FIG. 3. $I(\Omega)$ of the Kitaev models with $J_{x,y,z} = J$ and $\mathcal{E}_{dc} = 0.1J$ at (a) a weak laser intensity $\mathcal{E}_{ac}/J = 10^{-3}$ and (b) strong intensities of $\mathcal{E}_{ac}/J = 0.1, 0.15$, and 0.2 . Blue lines and dotted points are respectively results of the linear response (Kubo) theory and numerically-solved master equation [57]. $I(\Omega)$ is normalized with the maximum value of the Kubo formula. Panels (c) and (d) show DoSs of fermions corresponding to the cases (a) and (b), respectively. (e) SHG [$I(2\Omega)$] and (f) THG [$I(3\Omega)$] of the Kitaev model with $\mathcal{E}_{dc} = 0.1J$ in the space $(\mathcal{E}_{ac}, \Omega)$. The intensities, panels (e) and (f), are normalized with $I(\Omega)$ at $(\mathcal{E}_{ac}, \Omega) = (0.05J, 2J)$. The corresponding DoSs are depicted in panels (g) and (h).

for $E_{dc} \neq 0$, this dynamical symmetry is broken, and even-order HHG is allowed. We note that for $\kappa \neq 0$, the unitary operator \hat{U} is modified as $\hat{U} \rightarrow \hat{V}\hat{U}$, where \hat{V} is the time-reversal operator.

Thus, even-order HHG can be controlled by the static electric field E_{dc} through dimerization. Similar effects have been discussed in a spin chain [41] and in electronic systems [80–90], where E_{dc} induces electric current breaking the inversion symmetry. Being based only on symmetry, the dynamical symmetry argument is applicable to a wide class of perturbed Kitaev models. For example, the dynamical symmetry survives for $J_z \neq J_x = J_y$ while it breaks down for $J_x \neq J_y$. The magnetic anisotropy dependence of even-order harmonics is discussed in Supplemental Material [57]. In the following, we assume $E_{dc} \neq 0$ as necessary to ensure that even-order HHG are present.

Dependence of Laser Frequency and Intensity.— Next,

we consider the Ω and E_{ac} dependence of the HHG. Figures 3(a) and 3(b), respectively, show the Ω dependence of $I(\Omega)$ for weak ($\mathcal{E}_{\text{ac}} = 10^{-3}J$) and strong ($\mathcal{E}_{\text{ac}} = 0.1J, 0.15J, 0.2J$) THz pulses. In addition to the numerical result of the Lindblad equation, we plot that of the linear response theory (the Kubo formula) (see the Supplemental Material [57]). From the comparison between $I(\Omega)$ in Fig. 3(a) [Fig. 3(b)] and the fermion density of state (DoS) $\mathcal{D}(\omega)$ in Fig. 3(c) [Fig. 3(d)], we find that two-particle continuum spectra occur in the driven Kitaev model. This results from the ME coupling between an ac electric field (i.e., photon) and a pair of fermions with \mathbf{k} and $-\mathbf{k}$. This continuum indicates the existence of fermionic excitations in Kitaev magnets, and it differs qualitatively from usual ordered magnets, where one often observes a delta-functional peak due to magnons [91].

It is noteworthy that even the fundamental harmonic ($\omega = \Omega$) shows characteristics of the QSL in the strong THz pulse. Unlike in the weak pulse, the Kubo formula is no longer valid in the strong one in the deep nonperturbative regime. In this regime of $\mathcal{E}_{\text{ac}} \gtrsim 0.15J$, a new broad peak emerges in $I(\Omega)$ at $\Omega_{\text{peak}} \sim 4J$ [Fig. 3(b)], which is twice as large as the high DoS position. Namely, $I(\Omega)$ driven by intense pulses tells us the peak position of the DoS. For instance, $E_{\text{ac}} = 0.15J/\eta_{\text{ms}} \sim 3 \text{ MV/cm}$ for $J = 10 \text{ K}$ under the assumption of $\mathcal{E}_{\text{ac}} = g_0\mu_B E_{\text{ac}}/c$, and it indicates that currently-available THz laser is strong enough to observe such nonlinear optical spectra. We note that in Fig. 3(b), the increase of $I(\Omega)$ in the high- Ω range around $\Omega \sim 8J$ is owing to the factor Ω^4 in $I(\Omega)$.

The SHG and third harmonic generation (THG) spectra, $I(2\Omega)$ and $I(3\Omega)$, are depicted in Figs. 3(e) and 3(f). We find that broad peaks in $I(2\Omega)$ and $I(3\Omega)$ appear around $\Omega = \Omega_{\text{peak}}/2$ and $\Omega_{\text{peak}}/3$, respectively. This is a natural result, indicating that excitation processes creating fermions with a high DoS are dominant in HHG. Figure 3(h) shows that the peak frequency of the THG is slightly higher than that of the DoS $\mathcal{D}(3\Omega/2)$. This would also be attributed to the factor $(3\Omega)^4$ in $I(3\Omega)$.

Effect of DC Magnetic Field.— Now we discuss the dc-magnetic-field dependence of HHG in Kitaev models. We focus on the antiferromagnetic Kitaev model [57], where the Kitaev QSL state is more stable against magnetic fields than in the ferromagnetic case [92]. The magnetic-field driven κ term opens a mass gap Δ_κ in the fermion band, as shown in Fig. 1(g). As Δ_κ increases, the maximum of $\mathcal{D}(\omega)$ at $\omega \sim 2|J|$ grows up for $\Delta_\kappa \lesssim 2|J|$ ($\kappa \lesssim 0.2|J|$) [see Figs. 1(e) and 1(g)]. Therefore, the intensities of HHG spectra are expected to be controlled by the dc magnetic field and laser frequency Ω . Figure 4 proves this expectation. Panels (a) and (c), respectively, show the Ω dependence of $I(\Omega)$ and $\mathcal{D}(\omega)$ at a tuned effective magnetic field $\kappa = 0.2|J|$, where $\mathcal{D}(\Omega)$ take the

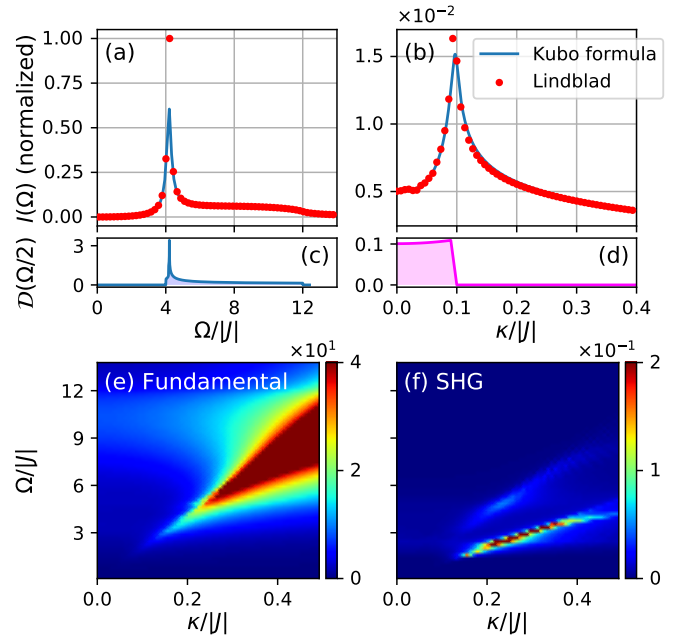


FIG. 4. (a) $I(\Omega)$ in an antiferromagnetic ($J < 0$) Kitaev model with $\kappa = 0.2|J|$, $\mathcal{E}_{\text{dc}} = 0$, and $\mathcal{E}_{\text{ac}} = 10^{-3}|J|$. (b) κ dependence of $I(\Omega)$ in $\Omega = 2.0|J|$, $\mathcal{E}_{\text{dc}} = 0$, and $\mathcal{E}_{\text{ac}} = 10^{-3}|J|$. Blue line and dotted points are respectively results of the linear response theory and the master equation [57]. $I(\Omega)$ in (a) and (b) are normalized with the maximum value in the panel (a). (c) Ω and (d) κ dependences of $\mathcal{D}(\omega)$ that respectively correspond to panels (a) and (b). (e) $I(\Omega)$ and (f) $I(2\Omega)$ of the Kitaev model with $\mathcal{E}_{\text{dc}} = \mathcal{E}_{\text{ac}} = 0.1|J|$. The intensities, panels (e) and (f), are normalized with $I(\Omega)$ at $(\kappa, \Omega) = (0.05|J|, 2|J|)$.

highest value at $\Omega_0 \sim \Delta_\kappa \sim 2|J|$. In this case, we have a sharp peak of $I(\Omega)$ at $\Omega_{\text{peak}} = 2\Omega_0 \sim 4|J|$. Figures 4(b) and 4(d) represent $I(\Omega)$ and $\mathcal{D}(\omega)$ as a functions of κ at a fixed $\Omega = 2|J|$. We see that a clear peak of $I(\Omega)$ appears when Δ_κ passes across one-half of the laser frequency $\Omega/2$.

We also show $I(\Omega)$ and $I(2\Omega)$ in the (κ, Ω) space in Figs. 4(e) and 4(f). For $I(\Omega)$ in the case of $\kappa \gtrsim 0.2|J|$, the frequency Ω of the broad peak increases monotonically in an almost κ -linear fashion. This is because the peak position Ω_0 of $\mathcal{D}(\Omega)$ increases almost linearly with κ for $\kappa \gtrsim 0.2|J|$ (for more details, see Fig. S15 of the Supplemental Material [57]). Since $\kappa \sim |\mathbf{B}|^3$, the \mathbf{B} -cube-dependent frequency at the peak is specific for the Kitaev model and essentially differs from the \mathbf{B} -linear behavior of magnon peaks. The frequency at the peak of $I(2\Omega)$ is almost half of Ω_{peak} of $I(\Omega)$, as shown in Fig. 4(f), and this is a natural result from the perturbative viewpoint. We note that, even in the linear response regime ($\omega = \Omega$ and weak THz pulse), the fundamental harmonic shows characteristics of the QSL for $\kappa \gtrsim 0.2|J|$ (see the Supplemental Material [57]). $I(\Omega)$ driven by intense pulses with a finite magnetic field tells

us the peak position of the DoS Ω_0 , which is half as large as Ω_{peak} .

Finally, we estimate the laser intensity required in the HHG experiment. For the Kitaev magnet with $|J|/k_B = 10\text{K}$ and $\kappa = 0$, the required ac electric field E_{ac} for the observation of HHG can be estimated from Fig. 2(a): $E_{\text{ac}} = 2.6\text{MV/cm}$ at 0.42THz is necessary for $R(\Omega) = I(2\Omega)/I(\Omega) \gtrsim 10^{-2}$ and $E_{\text{ac}} = 0.9\text{MV/cm}$ for $R(\Omega) \gtrsim 10^{-3}$. These required ac electric fields can be reduced when applying the effective static magnetic field $\kappa = 0.2|J|$ as shown in Fig. 4 and the Supplemental Material [57]. In this case, the electric field is estimated as $E_{\text{ac}} = 0.7\text{MV/cm}$ at 0.42THz for $R(\Omega) \gtrsim 10^{-2}$ and $E_{\text{ac}} = 0.2\text{MV/cm}$ for $R(\Omega) \gtrsim 10^{-3}$. We remark that the above criteria, $R(\Omega) \gtrsim 10^{-2}$ and 10^{-3} , for successful detection are much more strict than those in the actual experiments for electronic systems [51–53]. Thus, much weaker pulses might be enough to verify our predictions experimentally. These estimates indicate that lower-order harmonics in Kitaev magnets can be detected with current THz light techniques.

Conclusions.— We have analyzed the HHG in Kitaev magnets with an ME coupling by using a quantum master equation and the linear response theory. Our results show that the specific nature of the Majorana fermion excitations can be detected by linear and nonlinear THz-light responses. The characteristics of the Kitaev model, such as even-order harmonics, continuum HHG spectra, and broad peaks, can be controlled by applying static electric or magnetic fields. This study sheds light on an interdisciplinary field between photo science and QSLs.

Our setup does not accompany vison (localized fermion) excitations. Studies for laser-driven vison dynamics and the effects of temperature and ac Zeeman terms are interesting directions for future work.

M. S. was supported by JSPS KAKENHI (Grant No. 17K05513 and No. 20H01830) and a Grant-in-Aid for Scientific Research on Innovative Areas “Quantum Liquid Crystals” (Grant No. JP19H05825). T.N.I. was supported by JSPS KAKENHI Grant No. JP18K13495 and No. 21K13852.

* 20nm010t@vc.ibaraki.ac.jp

† tikedada@issp.u-tokyo.ac.jp

‡ masahiro.sato.phys@vc.ibaraki.ac.jp

- [1] X.-G. Wen, *Quantum Field Theory of Many-Body Systems* (Oxford University Press, Oxford, 2007).
- [2] L. Balents, Spin liquids in frustrated magnets, *Nature* **464**, 199 (2010).
- [3] L. Savary and L. Balents, Quantum spin liquids: a review, *Reports Prog. Phys.* **80**, 016502 (2017).
- [4] J. Knolle and R. Moessner, A Field Guide to Spin Liquids, *Annu. Rev. Condens. Matter Phys.* **10**, 451 (2019).
- [5] M. Yamashita, N. Nakata, Y. Senshu, M. Nagata, H. M. Yamamoto, R. Kato, T. Shibauchi, and Y. Matsuda, Highly mobile gapless excitations in a two-dimensional candidate quantum spin liquid, *Science* (80-.) **328**, 1246 (2010).
- [6] A. V. Sologubenko, K. Giannò, H. R. Ott, A. Vietkine, and A. Revcolevschi, Heat transport by lattice and spin excitations in the spin-chain compounds SrCuO₂ and Sr₂CuO₃, *Phys. Rev. B* **64**, 054412 (2001).
- [7] D. Hirobe, M. Sato, Y. Shiomi, H. Tanaka, and E. Saitoh, Magnetic thermal conductivity far above the Néel temperature in the Kitaev-magnet candidate α -RuCl₃, *Phys. Rev. B* **95**, 241112 (2017).
- [8] Y. Onose, T. Ideue, H. Katsura, Y. Shiomi, N. Nagaosa, and Y. Tokura, Observation of the magnon hall effect, *Science* (80-.) **329**, 297 (2010).
- [9] D. Watanabe, K. Sugii, M. Shimozawa, Y. Suzuki, T. Yajima, H. Ishikawa, Z. Hiroi, T. Shibauchi, Y. Matsuda, and M. Yamashita, Emergence of nontrivial magnetic excitations in a spin-liquid state of kagomé volborthite, *Proc. Natl. Acad. Sci. (U. S. A.)* **113**, 8653 (2016).
- [10] S. Trebst, Kitaev Materials, [arXiv:1701.07056](https://arxiv.org/abs/1701.07056).
- [11] M. Hermanns, I. Kimchi, and J. Knolle, Physics of the Kitaev Model: Fractionalization, Dynamic Correlations, and Material Connections, *Annu. Rev. Condens. Matter Phys.* **9**, 17 (2018).
- [12] H. Takagi, T. Takayama, G. Jackeli, G. Khaliullin, and S. E. Nagler, Concept and realization of Kitaev quantum spin liquids, *Nat. Rev. Phys.* **1**, 264 (2019).
- [13] Y. Motome and J. Nasu, Hunting Majorana Fermions in Kitaev Magnets, *J. Phys. Soc. Japan* **89**, 012002 (2020).
- [14] Y. Motome, R. Sano, S. Jang, Y. Sugita, and Y. Kato, Materials design of Kitaev spin liquids beyond the Jackeli–Khaliullin mechanism, *J. Phys. Condens. Matter* **32**, 404001 (2020).
- [15] Y. Kasahara, T. Ohnishi, Y. Mizukami, O. Tanaka, S. Ma, K. Sugii, N. Kurita, H. Tanaka, J. Nasu, Y. Motome, T. Shibauchi, and Y. Matsuda, Majorana quantization and half-integer thermal quantum Hall effect in a Kitaev spin liquid, *Nature* **559**, 227 (2018).
- [16] L. J. Sandilands, Y. Tian, K. W. Plumb, Y.-J. Kim, and K. S. Burch, Scattering Continuum and Possible Fractionalized Excitations in α -RuCl₃, *Phys. Rev. Lett.* **114**, 147201 (2015).
- [17] J. Nasu, J. Knolle, D. L. Kovrizhin, Y. Motome, and R. Moessner, Fermionic response from fractionalization in an insulating two-dimensional magnet, *Nat. Phys.* **12**, 912 (2016).
- [18] J. Xing, E. Feng, Y. Liu, E. Emmanouilidou, C. Hu, J. Liu, D. Graf, A. P. Ramirez, G. Chen, H. Cao, and N. Ni, Néel-type antiferromagnetic order and magnetic field–temperature phase diagram in the spin- $\frac{1}{2}$ rare-earth honeycomb compound YbCl₃, *Phys. Rev. B* **102**, 014427 (2020).
- [19] H. Hirori, A. Doi, F. Blanchard, and K. Tanaka, Single-cycle terahertz pulses with amplitudes exceeding 1 MV/cm generated by optical rectification in LiNbO₃, *Appl. Phys. Lett.* **98**, 091106 (2011).
- [20] M. Sato, T. Higuchi, N. Kanda, K. Konishi, K. Yoshioka, T. Suzuki, K. Misawa, and M. Kuwata-Gonokami, Terahertz polarization pulse shaping with arbitrary field control, *Nat. Photon.* **7**, 724 (2013).

- [21] S. S. Dhillon, M. S. Vitiello, E. H. Linfield, A. G. Davies, M. C. Hoffmann, J. Booske, C. Paoloni, M. Gensch, P. Weightman, G. P. Williams, E. Castro-Camus, D. R. S. Cumming, F. Simoens, I. Escorcia-Carranza, J. Grant, S. Lucyszyn, M. Kuwata-Gonokami, K. Konishi, M. Koch, C. A. Schmuttenmaer, T. L. Cocker, R. Huber, A. G. Markelz, Z. D. Taylor, V. P. Wallace, J. Axel Zeitler, J. Sibik, T. M. Korter, B. Ellison, S. Rea, P. Goldsmith, K. B. Cooper, R. Appleby, D. Pardo, P. G. Huggard, V. Krozer, H. Shams, M. Fice, C. Renaud, A. Seeds, A. Stöhr, M. Naftaly, N. Ridler, R. Clarke, J. E. Cunningham, and M. B. Johnston, The 2017 terahertz science and technology roadmap, *J. Phys. D* **50**, 043001 (2017).
- [22] B. Liu, H. Bromberger, A. Cartella, T. Gebert, M. Först, and A. Cavalleri, Generation of narrowband, high-intensity, carrier-envelope phase-stable pulses tunable between 4 and 18 THz, *Opt. Lett.* **42**, 129 (2017).
- [23] A. Pimenov, A. A. Mukhin, V. Y. Ivanov, V. D. Travkin, A. M. Balbashov, and A. Loidl, Possible evidence for electromagnons in multiferroic manganites, *Nat. Phys.* **2**, 97 (2006).
- [24] Y. Takahashi, R. Shimano, Y. Kaneko, H. Murakawa, and Y. Tokura, Magnetolectric resonance with electromagnons in a perovskite helimagnet, *Nat. Phys.* **8**, 121 (2012).
- [25] T. Kubacka, J. A. Johnson, M. C. Hoffmann, C. Vicario, S. de Jong, P. Beaud, S. Grubel, S. W. Huang, L. Huber, L. Patthey, Y. D. Chuang, J. J. Turner, G. L. Dakovski, W. S. Lee, M. P. Minitti, W. Schlotter, R. G. Moore, C. P. Hauri, S. M. Koohpayeh, V. Scagnoli, G. Ingold, S. L. Johnson, and U. Staub, Large-Amplitude Spin Dynamics Driven by a THz Pulse in Resonance with an Electromagnon, *Science* (80-.). **343**, 1333 (2014).
- [26] I. Kézsmárki, D. Szaller, S. Bordács, V. Kocsis, Y. Tokunaga, Y. Taguchi, H. Murakawa, Y. Tokura, H. Engelkamp, T. Rößm, and U. Nagel, One-way transparency of four-coloured spin-wave excitations in multiferroic materials, *Nat. Commun.* **5**, 3203 (2014).
- [27] Y. Mukai, H. Hirori, T. Yamamoto, H. Kageyama, and K. Tanaka, Nonlinear magnetization dynamics of antiferromagnetic spin resonance induced by intense terahertz magnetic field, *New J. Phys.* **18**, 013045 (2016).
- [28] S. Baierl, J. H. Mentink, M. Hohenleutner, L. Braun, T.-M. Do, C. Lange, A. Sell, M. Fiebig, G. Woltersdorf, T. Kampfrath, and R. Huber, Terahertz-Driven Nonlinear Spin Response of Antiferromagnetic Nickel Oxide, *Phys. Rev. Lett.* **117**, 197201 (2016).
- [29] J. Lu, X. Li, H. Y. Hwang, B. K. Ofori-Okai, T. Kurihara, T. Suemoto, and K. A. Nelson, Coherent Two-Dimensional Terahertz Magnetic Resonance Spectroscopy of Collective Spin Waves, *Phys. Rev. Lett.* **118**, 207204 (2017).
- [30] P. Němec, M. Fiebig, T. Kampfrath, and A. V. Kimel, Antiferromagnetic opto-spintronics, *Nat. Phys.* **14**, 229 (2018).
- [31] A. A. Sirenko, P. Marsik, C. Bernhard, T. N. Stanislavchuk, V. Kiryukhin, and S.-W. Cheong, Terahertz Vortex Beam as a Spectroscopic Probe of Magnetic Excitations, *Phys. Rev. Lett.* **122**, 237401 (2019).
- [32] S. Miyahara and N. Furukawa, Theory of electric field induced one-magnon resonance in cycloidal spin magnets, [arXiv:0811.4082](https://arxiv.org/abs/0811.4082).
- [33] M. Mochizuki and N. Nagaosa, Theoretically Predicted Picosecond Optical Switching of Spin Chirality in Multiferroics, *Phys. Rev. Lett.* **105**, 147202 (2010).
- [34] M. Mochizuki, N. Furukawa, and N. Nagaosa, Theory of Electromagnons in the Multiferroic Mn Perovskites: The Vital Role of Higher Harmonic Components of the Spiral Spin Order, *Phys. Rev. Lett.* **104**, 177206 (2010).
- [35] S. Miyahara and N. Furukawa, Nonreciprocal Directional Dichroism and Toroidal Magnons in Helical Magnets, *J. Phys. Soc. Japan* **81**, 023712 (2012).
- [36] S. Takayoshi, H. Aoki, and T. Oka, Magnetization and phase transition induced by circularly polarized laser in quantum magnets, *Phys. Rev. B* **90**, 085150 (2014).
- [37] S. Takayoshi, M. Sato, and T. Oka, Laser-induced magnetization curve, *Phys. Rev. B* **90**, 214413 (2014).
- [38] M. Sato, Y. Sasaki, and T. Oka, Floquet Majorana Edge Mode and Non-Abelian Anyons in a Driven Kitaev Model, [arXiv:1404.2010](https://arxiv.org/abs/1404.2010).
- [39] M. Sato, S. Takayoshi, and T. Oka, Laser-Driven Multiferroics and Ultrafast Spin Current Generation, *Phys. Rev. Lett.* **117**, 147202 (2016).
- [40] H. Fujita and M. Sato, Encoding orbital angular momentum of light in magnets, *Phys. Rev. B* **96**, 060407 (2017).
- [41] T. N. Ikeda and M. Sato, High-harmonic generation by electric polarization, spin current, and magnetization, *Phys. Rev. B* **100**, 214424 (2019).
- [42] H. Ishizuka and M. Sato, Rectification of Spin Current in Inversion-Asymmetric Magnets with Linearly Polarized Electromagnetic Waves, *Phys. Rev. Lett.* **122**, 197702 (2019).
- [43] H. Ishizuka and M. Sato, Theory for shift current of bosons: Photogalvanic spin current in ferrimagnetic and antiferromagnetic insulators, *Phys. Rev. B* **100**, 224411 (2019).
- [44] S. Higashikawa, H. Fujita, and M. Sato, Floquet engineering of classical systems, [arXiv:1810.01103](https://arxiv.org/abs/1810.01103).
- [45] S. Takayoshi, Y. Murakami, and P. Werner, High-harmonic generation in quantum spin systems, *Phys. Rev. B* **99**, 184303 (2019).
- [46] M. Sato and Y. Morisaku, Two-photon driven magnon-pair resonance as a signature of spin-nematic order, *Phys. Rev. B* **102**, 060401 (2020).
- [47] Y. Wan and N. P. Armitage, Resolving Continua of Fractional Excitations by Spinon Echo in THz 2D Coherent Spectroscopy, *Phys. Rev. Lett.* **122**, 257401 (2019).
- [48] W. Choi, K. H. Lee, and Y. B. Kim, Theory of Two-Dimensional Nonlinear Spectroscopy for the Kitaev Spin Liquid, *Phys. Rev. Lett.* **124**, 117205 (2020).
- [49] S. Ghimire, A. D. Dichiaro, E. Sistrunk, P. Agostini, L. F. Dimauro, and D. A. Reis, Observation of high-order harmonic generation in a bulk crystal, *Nat. Phys.* **7**, 1847 (2011).
- [50] O. Schubert, M. Hohenleutner, F. Langer, B. Urbanek, C. Lange, U. Huttner, D. Golde, T. Meier, M. Kira, S. W. Koch, and R. Huber, Sub-cycle control of terahertz high-harmonic generation by dynamical Bloch oscillations, *Nat. Photon.* **8**, 119 (2014).
- [51] H. A. Hafez, S. Kovalev, J.-C. Deinert, Z. Mics, B. Green, N. Awari, M. Chen, S. Germanskiy, U. Lehnert, J. Teichert, Z. Wang, K.-J. Tielrooij, Z. Liu, Z. Chen, A. Narita, K. Müllen, M. Bonn,

- M. Gensch, and D. Turchinovich, Extremely efficient terahertz high-harmonic generation in graphene by hot Dirac fermions, *Nature* **561**, 507 (2018).
- [52] B. Cheng, N. Kanda, T. N. Ikeda, T. Matsuda, P. Xia, T. Schumann, S. Stemmer, J. Itatani, N. P. Armitage, and R. Matsunaga, Efficient Terahertz Harmonic Generation with Coherent Acceleration of Electrons in the Dirac Semimetal Cd_3As_2 , *Phys. Rev. Lett.* **124**, 117402 (2020).
- [53] S. Kovalev, R. M. A. Dantas, S. Germanskiy, J.-C. Deinert, B. Green, I. Ilyakov, N. Awari, M. Chen, M. Bawatna, J. Ling, F. Xiu, P. H. M. van Loosdrecht, P. Surówka, T. Oka, and Z. Wang, Non-perturbative terahertz high-harmonic generation in the three-dimensional Dirac semimetal Cd_3As_2 , *Nat. Commun.* **11**, 2451 (2020).
- [54] Y. Tokura, S. Seki, and N. Nagaosa, Multiferroics of spin origin, *Reports Prog. Phys.* **77**, 076501 (2014).
- [55] H.-P. Breuer and F. Petruccione, *The Theory of Open Quantum Systems* (Oxford University Press, Oxford, 2007).
- [56] R. Alicki and K. Lendi, *Quantum Dynamical Semigroups and Applications*, Lecture Notes in Physics, Vol. 717 (Springer, Berlin, 2007).
- [57] See the Supplemental Material for additional details, such as the magnetic anisotropy dependence of even-order harmonics and the results in the ferromagnetic ($J > 0$) Kitaev model.
- [58] A. Kitaev, Anyons in an exactly solved model and beyond, *Ann. Phys.* **321**, 2 (2006).
- [59] D. Hüvonen, U. Nagel, T. Rööm, Y. J. Choi, C. L. Zhang, S. Park, and S.-W. Cheong, Magnetic excitations and optical transitions in the multiferroic spin- $\frac{1}{2}$ system LiCu_2O_2 , *Phys. Rev. B* **80**, 100402 (2009).
- [60] S. Furukawa, M. Sato, and S. Onoda, Chiral Order and Electromagnetic Dynamics in One-Dimensional Multiferroic Cuprates, *Phys. Rev. Lett.* **105**, 257205 (2010).
- [61] H.-D. Chen and Z. Nussinov, Exact results of the Kitaev model on a hexagonal lattice: spin states, string and brane correlators, and anyonic excitations, *J. Phys. A* **41**, 075001 (2008).
- [62] E. H. Lieb, Flux phase of the half-filled band, *Phys. Rev. Lett.* **73**, 2158 (1994).
- [63] D. Takikawa and S. Fujimoto, Impact of off-diagonal exchange interactions on the Kitaev spin-liquid state of $\alpha\text{-RuCl}_3$, *Phys. Rev. B* **99**, 224409 (2019).
- [64] D. Takikawa and S. Fujimoto, Topological phase transition to Abelian anyon phases due to off-diagonal exchange interaction in the Kitaev spin liquid state, *Phys. Rev. B* **102**, 174414 (2020).
- [65] As discussed in Ref. [63], if the Kitaev magnet has both a dc magnetic field and a sort of perturbative term, an additional three spin interaction appears and its coupling constant is possibly proportional to B . However, this paper has focused on the system with $\kappa \propto B^3$.
- [66] A. Kirilyuk, A. V. Kimel, and T. Rasing, Ultrafast optical manipulation of magnetic order, *Rev. Mod. Phys.* **82**, 2731 (2010).
- [67] M. Oshikawa and I. Affleck, Low-Temperature Electron Spin Resonance Theory for Half-Integer Spin Antiferromagnetic Chains, *Phys. Rev. Lett.* **82**, 5136 (1999).
- [68] M. Oshikawa and I. Affleck, Electron spin resonance in $S = \frac{1}{2}$ antiferromagnetic chains, *Phys. Rev. B* **65**, 134410 (2002).
- [69] S. C. Furuya and M. Sato, Electron Spin Resonance in Quasi-One-Dimensional Quantum Antiferromagnets: Relevance of Weak Interchain Interactions, *J. Phys. Soc. Japan* **84**, 033704 (2015).
- [70] E. Beaurepaire, J.-C. Merle, A. Daunois, and J.-Y. Bigot, Ultrafast Spin Dynamics in Ferromagnetic Nickel, *Phys. Rev. Lett.* **76**, 4250 (1996).
- [71] B. Koopmans, M. van Kampen, J. T. Kohlhepp, and W. J. M. de Jonge, Ultrafast Magneto-Optics in Nickel: Magnetism or Optics?, *Phys. Rev. Lett.* **85**, 844 (2000).
- [72] K. Lenz, H. Wende, W. Kuch, K. Baberschke, K. Nagy, and A. Jánossy, Two-magnon scattering and viscous Gilbert damping in ultrathin ferromagnets, *Phys. Rev. B* **73**, 144424 (2006).
- [73] C. Vittoria, S. D. Yoon, and A. Widom, Relaxation mechanism for ordered magnetic materials, *Phys. Rev. B* **81**, 014412 (2010).
- [74] E. A. Mashkovich, K. A. Grishunin, R. V. Mikhaylovskiy, A. K. Zvezdin, R. V. Pisarev, M. B. Strugatsky, P. C. M. Christianen, T. Rasing, and A. V. Kimel, Terahertz Optomagnetism: Nonlinear THz Excitation of GHz Spin Waves in Antiferromagnetic FeBO_3 , *Phys. Rev. Lett.* **123**, 157202 (2019).
- [75] C. Tzschaschel, T. Satoh, and M. Fiebig, Tracking the ultrafast motion of an antiferromagnetic order parameter, *Nat. Commun.* **10**, 3995 (2019).
- [76] J. D. Jackson, *Classical Electrodynamics* (Wiley, Weinheim, Germany, 1998).
- [77] O. E. Alon, V. Averbukh, and N. Moiseyev, Selection Rules for the High Harmonic Generation Spectra, *Phys. Rev. Lett.* **80**, 3743 (1998).
- [78] O. Neufeld, D. Podolsky, and O. Cohen, Floquet group theory and its application to selection rules in harmonic generation, *Nat. Commun.* **10**, 405 (2019).
- [79] T. Morimoto, H. C. Po, and A. Vishwanath, Floquet topological phases protected by time glide symmetry, *Phys. Rev. B* **95**, 195155 (2017).
- [80] J. B. Khurgin, Current induced second harmonic generation in semiconductors, *Appl. Phys. Lett.* **67**, 1113 (1995).
- [81] S. Wu, L. Mao, A. M. Jones, W. Yao, C. Zhang, and X. Xu, Quantum-Enhanced Tunable Second-Order Optical Nonlinearity in Bilayer Graphene, *Nano Lett.* **12**, 2032 (2012).
- [82] J. L. Cheng, N. Vermeulen, and J. E. Sipe, DC current induced second order optical nonlinearity in graphene, *Opt. Express* **22**, 15868 (2014).
- [83] O. A. Aktsipetrov, V. O. Bessonov, A. A. Fedyanin, and V. O. Val'dner, DC-induced generation of the reflected second harmonic in silicon, *JETP Lett.* **89**, 58 (2009).
- [84] B. A. Ruzicka, L. K. Werake, G. Xu, J. B. Khurgin, E. Y. Sherman, J. Z. Wu, and H. Zhao, Second-Harmonic Generation Induced by Electric Currents in GaAs, *Phys. Rev. Lett.* **108**, 077403 (2012).
- [85] A. Y. Bykov, T. V. Murzina, M. G. Rybin, and E. D. Obraztsova, Second harmonic generation in multilayer graphene induced by direct electric current, *Phys. Rev. B* **85**, 121413 (2012).
- [86] Y. Q. An, F. Nelson, J. U. Lee, and A. C. Diebold, Enhanced optical second-harmonic generation from the current-biased graphene/SiO₂/Si(001) structure, *Nano Lett.* **13**, 2104 (2013).

- [87] A. Moor, A. F. Volkov, and K. B. Efetov, Amplitude Higgs Mode and Admittance in Superconductors with a Moving Condensate, *Phys. Rev. Lett.* **118**, 047001 (2017).
- [88] S. Nakamura, Y. Iida, Y. Murotani, R. Matsunaga, H. Terai, and R. Shimano, Infrared Activation of the Higgs Mode by Supercurrent Injection in Superconducting NbN, *Phys. Rev. Lett.* **122**, 257001 (2019).
- [89] S. Nakamura, K. Katsumi, H. Terai, and R. Shimano, Nonreciprocal Terahertz Second-Harmonic Generation in Superconducting NbN under Supercurrent Injection, *Phys. Rev. Lett.* **125**, 097004 (2020).
- [90] K. Takasan, T. Morimoto, J. Orenstein, and J. E. Moore, Current-induced second harmonic generation in inversion-symmetric Dirac and Weyl semimetals, [arXiv:2007.08887](https://arxiv.org/abs/2007.08887).
- [91] Even a single-magnon spectrum can have a broad peak when its lifetime is short. In such a case, it becomes difficult to distinguish the Kitaev continuum and the broad magnon peak. However, combining the HHG experiment with an additional one, we can possibly distinguish these two excitations. For example, magnons always appear in an ordered phase which can be detected by a magnetic Bragg peak, a magnetic phase transition, etc.
- [92] J. Nasu, Y. Kato, Y. Kamiya, and Y. Motome, Successive Majorana topological transitions driven by a magnetic field in the Kitaev model, *Phys. Rev. B* **98**, 060416 (2018).

Supplemental Material: Linear and Nonlinear Optical Responses in Kitaev Spin Liquids

Minoru Kanega,¹ Tatsuhiko N. Ikeda,² Masahiro Sato¹

¹*Department of Physics, Ibaraki University, Mito, Ibaraki 310-8512, Japan*

²*Institute for Solid State Physics, University of Tokyo, Kashiwa, Chiba 277-8581, Japan*

S1. FERMIONIZATION OF KITAEV HONEYCOMB MODEL

In this section, we shortly review the fermionization of the Kitaev model [10–13, 58]. The Hamiltonian of the Kitaev model is given by

$$\begin{aligned}
 H_0 &= H_K + H_{\text{ms}} + H_\kappa \\
 &= -J \sum_{\alpha=\{x,y,z\}} \sum_{\langle \mathbf{r}, \mathbf{r}' \rangle_\alpha} \sigma_{\mathbf{r}}^\alpha \sigma_{\mathbf{r}'}^\alpha - \mathcal{E}_{\text{dc}} \left(- \sum_{\langle \mathbf{r}, \mathbf{r}' \rangle_x} \sigma_{\mathbf{r}}^x \sigma_{\mathbf{r}'}^x + \sum_{\langle \mathbf{r}, \mathbf{r}' \rangle_y} \sigma_{\mathbf{r}}^y \sigma_{\mathbf{r}'}^y \right) - \kappa \sum_{\text{NNN}} \sigma_{\mathbf{r}}^x \sigma_{\mathbf{r}'}^y \sigma_{\mathbf{r}''}^z,
 \end{aligned} \tag{S1.1}$$

where $\sigma_{\mathbf{r}}^\alpha$ is the α component of Pauli matrix on site \mathbf{r} . The first term H_K is the Kitaev exchange interaction on nearest-neighboring bonds. The second one $H_{\text{ms}} = E_{\text{dc}} \eta_{\text{ms}} (-\sum_{\langle \mathbf{r}, \mathbf{r}' \rangle_x} \sigma_{\mathbf{r}}^x \sigma_{\mathbf{r}'}^x + \sum_{\langle \mathbf{r}, \mathbf{r}' \rangle_y} \sigma_{\mathbf{r}}^y \sigma_{\mathbf{r}'}^y)$ with $\mathcal{E}_{\text{dc}} = E_{\text{dc}} \eta_{\text{ms}}$ is the dimerization energy driven by a static electric field E_{dc} along the \tilde{x} direction (see Fig. 1 in the main text). The dimerization is proportional to the electric polarization \hat{P} as

$$\hat{P} = \eta_{\text{ms}} \left(- \sum_{\langle \mathbf{r}, \mathbf{r}' \rangle_x} \sigma_{\mathbf{r}}^x \sigma_{\mathbf{r}'}^x + \sum_{\langle \mathbf{r}, \mathbf{r}' \rangle_y} \sigma_{\mathbf{r}}^y \sigma_{\mathbf{r}'}^y \right), \tag{S1.2}$$

where η_{ms} is the magnetoelectric (ME) coupling constant [54]. The final term H_κ is the three-spin term [58] driven by a static magnetic field \mathbf{B} , and we will explain H_κ in more detail later. This model can be fermionized by a Jordan–Wigner (JW) transformation, by regarding it as the array of one-dimensional chains consisting of the x and y bonds [61]. See Fig. S1. Through the JW transformation, the spin operators are rewritten by using spinless fermions

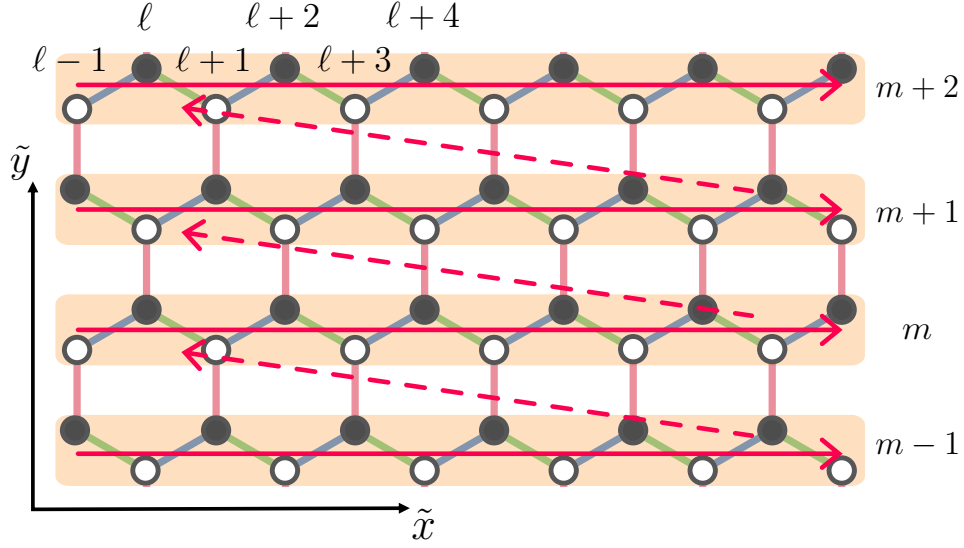


FIG. S1. Honeycomb lattice structure of the Kitaev model of Eq. (S1.1). Jordan–Wigner (JW) transformation is performed along the red lines.

as

$$\begin{cases} \sigma_{jk}^+ = c_{jk}^\dagger \exp \left[i\pi \left(\sum_{m=1}^{k-1} \sum_{\ell} c_{\ell m}^\dagger c_{\ell m} + \sum_{\ell=1}^{j-1} c_{\ell k}^\dagger c_{\ell k} \right) \right], \\ \sigma_{jk}^- = c_{jk} \exp \left[i\pi \left(\sum_{m=1}^{k-1} \sum_{\ell} c_{\ell m}^\dagger c_{\ell m} + \sum_{\ell=1}^{j-1} c_{\ell k}^\dagger c_{\ell k} \right) \right], \\ \sigma_{jk}^z = 2c_{jk}^\dagger c_{jk} - 1, \end{cases} \quad (\text{S1.3})$$

where $\sigma_{\mathbf{r}}^\pm = (\sigma_{\mathbf{r}}^x \pm i\sigma_{\mathbf{r}}^y)/2$. $c_{\mathbf{r}}^\dagger$ and $c_{\mathbf{r}}$ are respectively the spinless-fermion creation and annihilation operators that satisfy the anticommutation relations,

$$\{c_{\mathbf{r}}^\dagger, c_{\mathbf{r}'}\} = \delta_{\mathbf{r}\mathbf{r}'}, \quad \{c_{\mathbf{r}}^\dagger, c_{\mathbf{r}'}^\dagger\} = 0, \quad \{c_{\mathbf{r}}, c_{\mathbf{r}'}\} = 0. \quad (\text{S1.4})$$

First, we apply the JW transformation (S1.3) to $H_K + H_{\text{ms}}$:

$$\begin{aligned} H_K + H_{\text{ms}} = & -(J - \mathcal{E}_{\text{dc}}) \sum_{\langle \mathbf{r}, \mathbf{r}' \rangle_x} ((c_{\mathbf{r}}^a)^\dagger - c_{\mathbf{r}}^a) ((c_{\mathbf{r}'}^b)^\dagger + c_{\mathbf{r}'}^b) + (J + \mathcal{E}_{\text{dc}}) \sum_{\langle \mathbf{r}, \mathbf{r}' \rangle_y} ((c_{\mathbf{r}}^b)^\dagger + c_{\mathbf{r}}^b) ((c_{\mathbf{r}'}^a)^\dagger - c_{\mathbf{r}'}^a) \\ & - J \sum_{\langle \mathbf{r}, \mathbf{r}' \rangle_z} ((c_{\mathbf{r}}^b)^\dagger - c_{\mathbf{r}}^b) ((c_{\mathbf{r}}^b)^\dagger + c_{\mathbf{r}}^b) ((c_{\mathbf{r}'}^a)^\dagger - c_{\mathbf{r}'}^a) ((c_{\mathbf{r}'}^a)^\dagger + c_{\mathbf{r}'}^a). \end{aligned} \quad (\text{S1.5})$$

In Eq. (S1.5), the symbol \mathbf{r} is re-defined as a vector pointing to the bond center of z bond, and the index a (b) denotes the sublattice a (b) on the same z bond, as shown in Fig. S2(a). Here, we introduce the Majorana (real) fermion from the linear combination of $c_{\mathbf{r}}^\dagger$ and $c_{\mathbf{r}}$:

$$\begin{aligned} \xi_{\mathbf{r}}^a &= \frac{(c_{\mathbf{r}}^a - (c_{\mathbf{r}}^a)^\dagger)}{i}, & \chi_{\mathbf{r}}^a &= (c_{\mathbf{r}}^a + (c_{\mathbf{r}}^a)^\dagger), \\ \chi_{\mathbf{r}}^b &= \frac{(c_{\mathbf{r}}^b - (c_{\mathbf{r}}^b)^\dagger)}{i}, & \xi_{\mathbf{r}}^b &= (c_{\mathbf{r}}^b + (c_{\mathbf{r}}^b)^\dagger). \end{aligned} \quad (\text{S1.6})$$

Substituting Eq. (S1.6) into Eq. (S1.5), we can rewrite Hamiltonian (S1.5) as

$$H_K + H_{\text{ms}} = i(J - \mathcal{E}_{\text{dc}}) \sum_{\langle \mathbf{r}, \mathbf{r}' \rangle_x} \xi_{\mathbf{r}}^a \xi_{\mathbf{r}'}^b - i(J + \mathcal{E}_{\text{dc}}) \sum_{\langle \mathbf{r}, \mathbf{r}' \rangle_y} \xi_{\mathbf{r}}^b \xi_{\mathbf{r}'}^a - iJ \sum_{\langle \mathbf{r}, \mathbf{r}' \rangle_z} \alpha_{\mathbf{r}} \xi_{\mathbf{r}}^b \xi_{\mathbf{r}'}^a, \quad (\text{S1.7})$$

where $\alpha_{\mathbf{r}} = i\chi_{\mathbf{r}}^b \chi_{\mathbf{r}'}^a$, with \mathbf{r} and \mathbf{r}' being on a z bond. The operator $\alpha_{\mathbf{r}}$ in each z bond is the local conserved quantity and has eigenvalues 1 or -1 . In the ground state, the spatial distribution of the eigenvalue of $\{\alpha_{\mathbf{r}}\}$ is shown to be all unity (or all -1) [62]. Therefore, the pair $(\xi_{\mathbf{r}}^b, \xi_{\mathbf{r}'}^a)$ correspond to itinerant (dispersive) fermions, while the remaining fermions $(\chi_{\mathbf{r}}^b, \chi_{\mathbf{r}'}^a)$ are localized excitations (called vison). The vison has no dynamics and its excitation gap is estimated as $\sim 0.07|J|$ in the isotropic Kitaev model with $J_{x,y,z} = J$ [58]. From these arguments, the ground-state Hamiltonian (i.e., zero temperature $T = 0$) is described by only the itinerant Majorana fermions. We note that if we perform the perturbation theory for some of realistic perturbations, such as Heisenberg-term

$$H_{J_H} = J_H \sum_{\langle \mathbf{r}, \mathbf{r}' \rangle} \boldsymbol{\sigma}_{\mathbf{r}} \cdot \boldsymbol{\sigma}_{\mathbf{r}'}, \quad (\text{S1.8})$$

Γ -term

$$H_{\Gamma} = -\Gamma \sum_{\substack{\alpha, \beta, \gamma = \{x, y, z\} \\ \beta \neq \alpha, \gamma \neq \alpha}} \sum_{\langle \mathbf{r}, \mathbf{r}' \rangle_{\alpha}} \left[\sigma_{\mathbf{r}}^{\beta} \sigma_{\mathbf{r}'}^{\gamma} + \sigma_{\mathbf{r}}^{\gamma} \sigma_{\mathbf{r}'}^{\beta} \right], \quad (\text{S1.9})$$

and Γ' -term

$$H_{\Gamma'} = -\Gamma' \sum_{\substack{\alpha, \beta = \{x, y, z\} \\ \beta \neq \alpha}} \sum_{\langle \mathbf{r}, \mathbf{r}' \rangle_{\alpha}} \left[\sigma_{\mathbf{r}}^{\alpha} \sigma_{\mathbf{r}'}^{\beta} + \sigma_{\mathbf{r}}^{\beta} \sigma_{\mathbf{r}'}^{\alpha} \right], \quad (\text{S1.10})$$

their leading terms can be mapped to itinerant Majorana fermions [63, 64]. Namely, such perturbed Kitaev models can also be analyzed by using the fermionization. We note that the three-spin κ term is also derived from the third-order perturbation calculation in terms of a standard Zeeman interaction [58].

In the present study, we can choose $\alpha_{\mathbf{r}} = 1$ without loss of generality, and focus on the ground state below. From

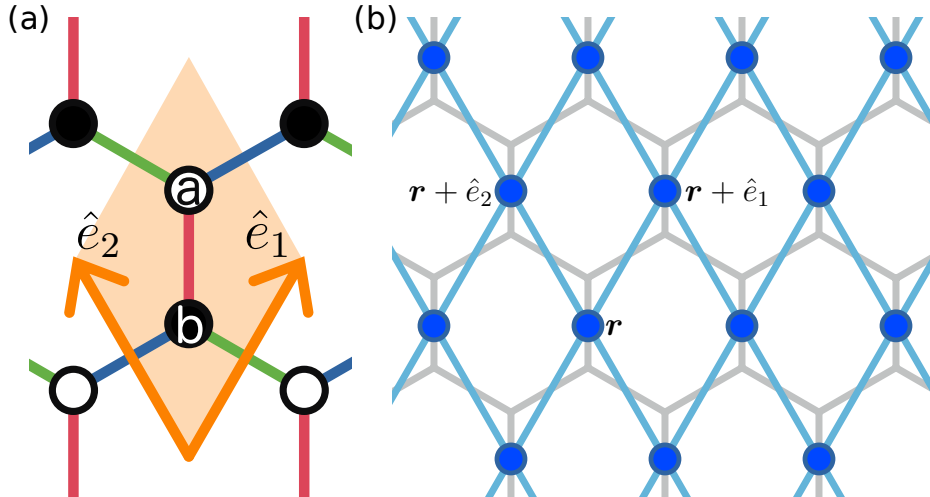


FIG. S2. (a) Unitcell of the Kitaev model. \hat{e}_1 and \hat{e}_2 are primitive translation vectors. (b) Lattice structure for the complex fermions $d_{\mathbf{r}}$ of the Kitaev model. The fermion $d_{\mathbf{r}}$ is defined on the virtual site (blue site) which is the bond center of each z bond.

the itinerant Majorana fermions, we define a complex fermion on the new site \mathbf{r} which is center of each z bond [see

Fig. S2(b)]:

$$\begin{cases} d_{\mathbf{r}} = \frac{1}{2}(\xi_{\mathbf{r}}^b + i\xi_{\mathbf{r}}^a), \\ d_{\mathbf{r}}^\dagger = \frac{1}{2}(\xi_{\mathbf{r}}^b - i\xi_{\mathbf{r}}^a), \end{cases} \quad (\text{S1.11})$$

where $d_{\mathbf{r}}^\dagger$ and $d_{\mathbf{r}}$ are respectively the spinless-fermion creation and annihilation operators that satisfy the anticommutation relations,

$$\{d_{\mathbf{r}}^\dagger, d_{\mathbf{r}'}\} = \delta_{\mathbf{r}\mathbf{r}'}, \quad \{d_{\mathbf{r}}^\dagger, d_{\mathbf{r}'}^\dagger\} = 0, \quad \{d_{\mathbf{r}}, d_{\mathbf{r}'}\} = 0. \quad (\text{S1.12})$$

Substituting Eq. (S1.11) into Eq. (S1.7), we represent the ground-state Hamiltonian with $\{\alpha_{\mathbf{r}}\} = 1$ as

$$H_K + H_{\text{ms}} = - \sum_{\mathbf{r}} \left[(J - \mathcal{E}_{\text{dc}})(d_{\mathbf{r}}^\dagger - d_{\mathbf{r}})(d_{\mathbf{r}+\hat{e}_1}^\dagger + d_{\mathbf{r}+\hat{e}_1}) + (J + \mathcal{E}_{\text{dc}})(d_{\mathbf{r}}^\dagger - d_{\mathbf{r}})(d_{\mathbf{r}+\hat{e}_2}^\dagger + d_{\mathbf{r}+\hat{e}_2}) + J(2d_{\mathbf{r}}^\dagger d_{\mathbf{r}} - 1) \right], \quad (\text{S1.13})$$

where \hat{e}_1 and \hat{e}_2 are primitive translation vectors of the Kitaev model, as shown in Fig. S2. Through Fourier transformation for the complex fermion $d_{\mathbf{r}}$,

$$d_{\mathbf{r}} = \frac{1}{\sqrt{N}} \sum_{\mathbf{k}} \tilde{d}_{\mathbf{k}} e^{i\mathbf{k}\cdot\mathbf{r}}, \quad (\text{S1.14})$$

we obtain

$$H_K + H_{\text{ms}} = \sum_{\substack{\mathbf{k} \\ k_x > 0}} \left[\epsilon_{\mathbf{k}} \tilde{d}_{\mathbf{k}}^\dagger \tilde{d}_{\mathbf{k}} - \epsilon_{\mathbf{k}} \tilde{d}_{-\mathbf{k}} \tilde{d}_{-\mathbf{k}}^\dagger - i\Delta_{\mathbf{k}}^0 (\tilde{d}_{\mathbf{k}}^\dagger \tilde{d}_{-\mathbf{k}}^\dagger - \tilde{d}_{-\mathbf{k}} \tilde{d}_{\mathbf{k}}) \right], \quad (\text{S1.15})$$

where $\mathbf{k} = (k_x, k_y)^\top$ is a wave vector. $k_x = 2\pi(n/N_1 - m/N_2)/\sqrt{3}$ and $k_y = 2\pi(n/N_1 + m/N_2)/3$ ($n, m \in \mathbb{Z}$) are respectively the wave numbers along the \tilde{x} and \tilde{y} directions, where $N = N_1 N_2$ is the total number of unit cells and $N_{1(2)}$ is the size along the $\hat{e}_{1(2)}$ direction. The parameters $\epsilon_{\mathbf{k}}$ and $\Delta_{\mathbf{k}}^0$ are respectively defined as $\epsilon_{\mathbf{k}} = \epsilon_{\mathbf{k}}^{\text{iso}} - E_{\text{dc}} \epsilon_{\mathbf{k}}^P$ and $\Delta_{\mathbf{k}}^0 = \Delta_{\mathbf{k}}^{\text{iso}} - E_{\text{dc}} \Delta_{\mathbf{k}}^P$, in which

$$\epsilon_{\mathbf{k}}^{\text{iso}} = -2J(1 + \cos(\mathbf{k} \cdot \hat{e}_1) + \cos(\mathbf{k} \cdot \hat{e}_2)), \quad (\text{S1.16})$$

$$\Delta_{\mathbf{k}}^{\text{iso}} = 2J(\sin(\mathbf{k} \cdot \hat{e}_1) + \sin(\mathbf{k} \cdot \hat{e}_2)), \quad (\text{S1.17})$$

$$\epsilon_{\mathbf{k}}^P = -2\eta_{\text{ms}}(\cos(\mathbf{k} \cdot \hat{e}_1) - \cos(\mathbf{k} \cdot \hat{e}_2)), \quad (\text{S1.18})$$

$$\Delta_{\mathbf{k}}^P = 2\eta_{\text{ms}}(\sin(\mathbf{k} \cdot \hat{e}_1) - \sin(\mathbf{k} \cdot \hat{e}_2)). \quad (\text{S1.19})$$

For simplicity, hereafter we will rewrite $\sum_{\mathbf{k}, k_x > 0}$ as $\sum'_{\mathbf{k}}$.

Next let us consider the three-spin interaction H_κ . Each honeycomb plaquette has six kinds of three-spin terms defined on six trios consisting of three neighboring sites: $\{1, 2, 3\}$, $\{2, 3, 4\}$, $\{3, 4, 5\}$, $\{4, 5, 6\}$, $\{5, 6, 1\}$, and $\{6, 1, 2\}$. These six triplets are shown in Fig. S3(a). Following the fashion respecting the honeycomb plaquettes, we represent the three-spin interaction H_κ as

$$H_\kappa = -\kappa \sum_{\mathbf{p}} \left(\sigma_{\mathbf{p},1a}^x \sigma_{\mathbf{p},2b}^z \sigma_{\mathbf{p},3a}^y + \sigma_{\mathbf{p},6b}^z \sigma_{\mathbf{p},1a}^y \sigma_{\mathbf{p},2b}^x + \sigma_{\mathbf{p},2b}^y \sigma_{\mathbf{p},3a}^x \sigma_{\mathbf{p},4b}^z \right. \\ \left. + \sigma_{\mathbf{p},4b}^x \sigma_{\mathbf{p},5a}^z \sigma_{\mathbf{p},6b}^y + \sigma_{\mathbf{p},5a}^x \sigma_{\mathbf{p},4b}^y \sigma_{\mathbf{p},3a}^z + \sigma_{\mathbf{p},1a}^z \sigma_{\mathbf{p},6b}^x \sigma_{\mathbf{p},5a}^y \right), \quad (\text{S1.20})$$

where $\sum_{\mathbf{p}}$ means the sum over all the plaquettes. Through the JW transformation, it can be mapped to the next-nearest-neighboring (NNN) hopping terms of Majorana fermions (see Fig. S3(b)),

$$H_\kappa = -\kappa \sum_{\mathbf{p}} i \left(\xi_{\mathbf{p}}^{6b} \zeta_{\mathbf{p}}^{4b} + \alpha_{\mathbf{p},6-1} \xi_{\mathbf{p}}^{2b} \zeta_{\mathbf{p}}^{6b} + \alpha_{\mathbf{p},4-3} \xi_{\mathbf{p}}^{4b} \zeta_{\mathbf{p}}^{2b} \right. \\ \left. + \xi_{\mathbf{p}}^{3a} \zeta_{\mathbf{p}}^{1a} + \alpha_{\mathbf{p},4-3} \xi_{\mathbf{p}}^{5a} \zeta_{\mathbf{p}}^{3a} + \alpha_{\mathbf{p},6-1} \xi_{\mathbf{p}}^{1a} \zeta_{\mathbf{p}}^{5a} \right), \quad (\text{S1.21})$$

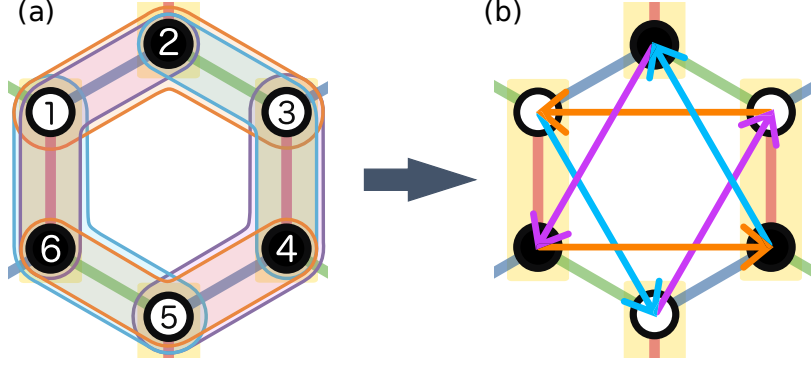


FIG. S3. (a) Six kinds of three-spin interactions in each plaquette. Three-spin interactions are defined on trios of three neighboring sites: $\{1, 2, 3\}$, $\{2, 3, 4\}$, $\{3, 4, 5\}$, $\{4, 5, 6\}$, $\{5, 6, 1\}$, and $\{6, 1, 2\}$. (b) Fermionized κ term in a plaquette. Each three-spin term is mapped to a next-nearest neighboring hopping with an imaginary factor. Namely, the three-spin term provides an effective “magnetic flux” for spinless fermions.

where $\alpha_{p,4-3} = i\chi_p^{4b}\chi_p^{3a}$ and $\alpha_{p,6-1} = i\chi_p^{6b}\chi_p^{1a}$. In the ground state, its complex-fermion representation is given by

$$H_\kappa = -i\kappa \sum_{\mathbf{r}} \left[\left(d_{\mathbf{r}+\hat{e}_2} + d_{\mathbf{r}+\hat{e}_2}^\dagger \right) \left(d_{\mathbf{r}+\hat{e}_1} + d_{\mathbf{r}+\hat{e}_1}^\dagger \right) + \left(d_{\mathbf{r}+\hat{e}_1} + d_{\mathbf{r}+\hat{e}_1}^\dagger \right) \left(d_{\mathbf{r}} + d_{\mathbf{r}}^\dagger \right) + \left(d_{\mathbf{r}} + d_{\mathbf{r}}^\dagger \right) \left(d_{\mathbf{r}+\hat{e}_2} + d_{\mathbf{r}+\hat{e}_2}^\dagger \right) \right. \\ \left. - \left(d_{\mathbf{r}-\hat{e}_2} - d_{\mathbf{r}-\hat{e}_2}^\dagger \right) \left(d_{\mathbf{r}-\hat{e}_1} - d_{\mathbf{r}-\hat{e}_1}^\dagger \right) - \left(d_{\mathbf{r}-\hat{e}_1} - d_{\mathbf{r}-\hat{e}_1}^\dagger \right) \left(d_{\mathbf{r}} - d_{\mathbf{r}}^\dagger \right) - \left(d_{\mathbf{r}} - d_{\mathbf{r}}^\dagger \right) \left(d_{\mathbf{r}-\hat{e}_2} - d_{\mathbf{r}-\hat{e}_2}^\dagger \right) \right], \quad (\text{S1.22})$$

where we have used $\{\alpha_{\mathbf{r}}\} = 1$. Since this NNN hopping have an imaginary factor $\propto i\kappa$, it plays the role of an effective “magnetic flux” for the fermion $\{d_{\mathbf{r}}\}$. Applying Fourier transformation to Eq. (S1.22), we obtain

$$H_\kappa = \sum_{\mathbf{k}}' \Delta_{\mathbf{k}}^B \left(\tilde{d}_{\mathbf{k}}^\dagger \tilde{d}_{-\mathbf{k}}^\dagger + \tilde{d}_{-\mathbf{k}} \tilde{d}_{\mathbf{k}} \right), \quad (\text{S1.23})$$

where

$$\Delta_{\mathbf{k}}^B = 4\kappa \left[\sin(\sqrt{3}k_x) - \sin(\mathbf{k} \cdot \hat{e}_1) + \sin(\mathbf{k} \cdot \hat{e}_2) \right]. \quad (\text{S1.24})$$

From Eqs. (S1.15) and (S1.23), the Hamiltonian $H_0 = H_K + H_{\text{ms}} + H_\kappa$ is expressed in the following matrix form,

$$H_0 = \sum_{\mathbf{k}}' \mathbf{D}_{\mathbf{k}}^\dagger M_{\mathbf{k}} \mathbf{D}_{\mathbf{k}}, \quad (\text{S1.25})$$

where

$$M_{\mathbf{k}} = \begin{pmatrix} \epsilon_{\mathbf{k}} & \Delta_{\mathbf{k}} \\ \Delta_{\mathbf{k}}^* & -\epsilon_{\mathbf{k}} \end{pmatrix}, \quad \mathbf{D}_{\mathbf{k}} = \begin{pmatrix} \tilde{d}_{\mathbf{k}} & \tilde{d}_{-\mathbf{k}}^\dagger \end{pmatrix}^\top, \quad (\text{S1.26})$$

with $\Delta_{\mathbf{k}} = -i\Delta_{\mathbf{k}}^0 + \Delta_{\mathbf{k}}^B$. This is the same form as that of a BCS Hamiltonian for superconductors. Through unitary transformation $\begin{pmatrix} f_{\mathbf{k}} & f_{-\mathbf{k}}^\dagger \end{pmatrix}^\top = U_{\mathbf{k}}^\dagger \mathbf{D}_{\mathbf{k}}$, Eq. (S1.25) is diagonalized as

$$H_0 = \sum_{\mathbf{k}}' E_{\mathbf{k}} (f_{\mathbf{k}}^\dagger f_{\mathbf{k}} + f_{-\mathbf{k}} f_{-\mathbf{k}}^\dagger), \quad (\text{S1.27})$$

with the energy band

$$E_{\mathbf{k}} = \sqrt{\epsilon_{\mathbf{k}}^2 + |\Delta_{\mathbf{k}}|^2}. \quad (\text{S1.28})$$

We have introduced new fermions $\{f_{\mathbf{k}}\}$ and unitary matrices $U_{\mathbf{k}}$. The ground state is given by

$$|\text{gs}\rangle = \prod'_{\mathbf{k}} (u_{\mathbf{k}} - v_{\mathbf{k}} \tilde{d}_{\mathbf{k}}^{\dagger} \tilde{d}_{-\mathbf{k}}^{\dagger}) |0\rangle, \quad (\text{S1.29})$$

with

$$u_{\mathbf{k}} = \sqrt{\frac{1}{2} \left(1 + \frac{\epsilon_{\mathbf{k}}}{E_{\mathbf{k}}}\right)}, \quad v_{\mathbf{k}} = \frac{\Delta_{\mathbf{k}}}{|\Delta_{\mathbf{k}}|} \sqrt{\frac{1}{2} \left(1 - \frac{\epsilon_{\mathbf{k}}}{E_{\mathbf{k}}}\right)}, \quad (\text{S1.30})$$

where $\prod'_{\mathbf{k}} = \prod_{\mathbf{k}, k_x > 0}$, and $|0\rangle$ is the Fock vacuum for the fermion $\{\tilde{d}_{\mathbf{k}}\}$.

The electric polarization \hat{P} can also be fermionized through JW transformation since it is a part of the Hamiltonian. The result is as follows:

$$\hat{P} = \sum'_{\mathbf{k}} \mathbf{D}_{\mathbf{k}}^{\dagger} P_{\mathbf{k}} \mathbf{D}_{\mathbf{k}}, \quad (\text{S1.31})$$

with

$$P_{\mathbf{k}} = \begin{pmatrix} \epsilon_{\mathbf{k}}^P & -i\Delta_{\mathbf{k}}^P \\ i\Delta_{\mathbf{k}}^P & -\epsilon_{\mathbf{k}}^P \end{pmatrix}. \quad (\text{S1.32})$$

S2. GROUND STATE ENERGY AND DC ELECTRIC FIELD DEPENDENCE

From the above section, the Hamiltonian of the Kitaev model is fermionized as

$$H_0 = \sum'_{\mathbf{k}} E_{\mathbf{k}} (f_{\mathbf{k}}^{\dagger} f_{\mathbf{k}} + f_{-\mathbf{k}}^{\dagger} f_{-\mathbf{k}}) - \sum'_{\mathbf{k}} E_{\mathbf{k}}. \quad (\text{S2.1})$$

Therefore, the ground-state energy per one unit cell is given by $E_{\text{GS}} = -N^{-1} \sum'_{\mathbf{k}} E_{\mathbf{k}}$ with N being the total number of unit cells. From the numerical calculation of E_{GS} , we plot the ground-state energy as the function of dc electric field E_{dc} in Fig. S4. It shows that if a dc electric field is applied, the energy decreases with being proportional to $\mathcal{E}_{\text{dc}}^2$. This means that when the system is distorted by a dc electric field E_{dc} , the electric state becomes more stable. This

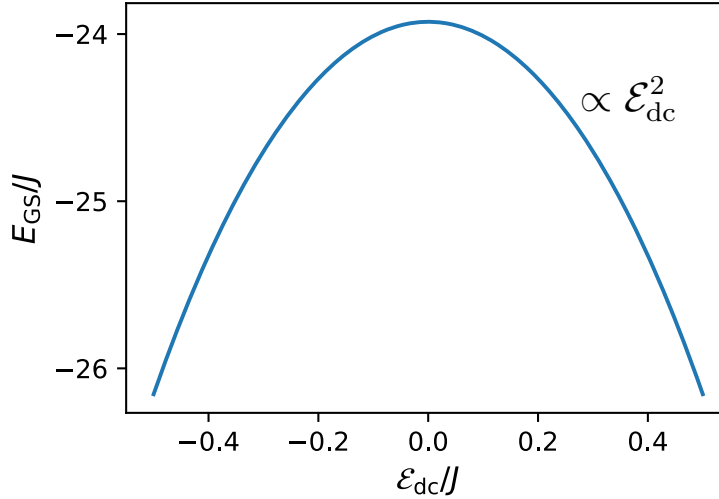


FIG. S4. \mathcal{E}_{dc} dependence of the ground-state energy E_{GS} in the Kitaev model with $\kappa = 0$.

result is consistent with our assumption that the dimerization is coupled to an applied electric field, and it indicates that the ME coupling can appear in a class of Kitaev-magnet candidates.

S3. TIME EVOLUTION OF DENSITY MATRIX VIA LINDBLAD EQUATION

In this section, we explain the quantum master equation approach [41, 46, 55, 56] to our driven Kitaev model. We consider a Kitaev model under the ac ME coupling between the polarization and an applied ac electric field $E_{ac}(t)$ along the \tilde{x} direction. The time-dependent Hamiltonian is given by

$$H(t) = H_0 - E_{ac}(t)\hat{P}. \quad (\text{S3.1})$$

Hereafter, we choose two vectors $\tilde{d}_{\mathbf{k}}^\dagger \tilde{d}_{-\mathbf{k}}^\dagger |0_{\mathbf{k}}\rangle$ and $|0_{\mathbf{k}}\rangle$ as the bases in each subspace with \mathbf{k} . Here, $|0_{\mathbf{k}}\rangle$ is the vacuum of the fermion $\tilde{d}_{\mathbf{k}}$. Using these bases, we can express the Hamiltonian (S3.1) in the 2×2 form,

$$H(t) = \sum_{\mathbf{k}}' \left[\begin{pmatrix} \epsilon_{\mathbf{k}} & \Delta_{\mathbf{k}} \\ \Delta_{\mathbf{k}}^* & -\epsilon_{\mathbf{k}} \end{pmatrix} - E_{ac}(t) \begin{pmatrix} \epsilon_{\mathbf{k}}^P & -i\Delta_{\mathbf{k}}^P \\ i\Delta_{\mathbf{k}}^P & -\epsilon_{\mathbf{k}}^P \end{pmatrix} \right] = \sum_{\mathbf{k}}' (M_{\mathbf{k}} - E_{ac}(t)P_{\mathbf{k}}). \quad (\text{S3.2})$$

We note that in our setup, there is no vison dynamics even when the laser is applied. Namely, the Hamiltonian for the laser-driven dynamics includes only itinerant Majorana fermions.

To describe the realistic non-equilibrium dynamics for the driven Kitaev model, we use the following quantum master equation of the Lindblad form [41, 46, 55, 56]

$$\frac{d\rho(\mathbf{k}, t)}{dt} = -i[h(\mathbf{k}, t), \rho(\mathbf{k}, t)] + \gamma \left(L_{\mathbf{k}}\rho(\mathbf{k}, t)L_{\mathbf{k}}^\dagger - \frac{1}{2} \{ L_{\mathbf{k}}^\dagger L_{\mathbf{k}}, \rho(\mathbf{k}, t) \} \right), \quad (\text{S3.3})$$

where $\rho(\mathbf{k}, t)$ is the density matrix in the \mathbf{k} subspace. $h(\mathbf{k}, t) = M_{\mathbf{k}} - E_{ac}(t)P_{\mathbf{k}}$ is the Hamiltonian in the \mathbf{k} subspace and the first commutator of Eq. (S3.3) represents the unitary dynamics caused by the Hamiltonian. The second γ term describes the dissipation dynamics, and it is necessary to describe ac-field driven phenomena in materials because dissipation effect is usually inevitable in most of matter. We set Lindblad operator $L_{\mathbf{k}}$ to be

$$L_{\mathbf{k}} = |g_{\mathbf{k}}\rangle \langle e_{\mathbf{k}}|, \quad (\text{S3.4})$$

where $|g_{\mathbf{k}}\rangle = (-v_{\mathbf{k}}, u_{\mathbf{k}})^\top$ and $|e_{\mathbf{k}}\rangle = (u_{\mathbf{k}}, v_{\mathbf{k}}^*)^\top$ are respectively ground and excited states of the static part of the Hamiltonian in the subspace \mathbf{k} . The Lindblad operator describes the relaxation to the ground state, and $1/\gamma$ is viewed as the relaxation time. For simplicity, we have assumed that the relaxation processes in multiple subspaces with different \mathbf{k} are independent of each other, and we have used a single value of γ for the total system. Unless otherwise stated throughout this work, we use a typical value $\gamma = 0.1J$, which corresponds to the relaxation time $\tau = 1/\gamma \sim 7.6$ ps for $J/k_B = 10$ K. We will shortly discuss the relaxation-rate dependence of the HHG spectra in Sec. S4. The initial density matrix $\rho(\mathbf{k}, t_{ini})$ at time $t = t_{ini}$ is set to be

$$\rho(\mathbf{k}, t_{ini}) = |g_{\mathbf{k}}\rangle \langle g_{\mathbf{k}}|. \quad (\text{S3.5})$$

To simplify the description, we perform a unitary transformation to the Lindblad equation (S3.3) with the unitary matrix

$$U_{\mathbf{k}} = (|e_{\mathbf{k}}\rangle |g_{\mathbf{k}}\rangle) = \begin{pmatrix} u_{\mathbf{k}} & -v_{\mathbf{k}} \\ v_{\mathbf{k}}^* & u_{\mathbf{k}} \end{pmatrix}, \quad (\text{S3.6})$$

which makes the matrix $M_{\mathbf{k}}$ diagonalized. Using $U_{\mathbf{k}}$, we define some matrices as follows:

$$\begin{cases} U_{\mathbf{k}}^\dagger \rho(\mathbf{k}, t) U_{\mathbf{k}} = \tilde{\rho}(\mathbf{k}, t), \\ U_{\mathbf{k}}^\dagger M_{\mathbf{k}} U_{\mathbf{k}} = \begin{pmatrix} E_{\mathbf{k}} & 0 \\ 0 & -E_{\mathbf{k}} \end{pmatrix} = \tilde{M}_{\mathbf{k}}, \\ U_{\mathbf{k}}^\dagger P_{\mathbf{k}} U_{\mathbf{k}} = \begin{pmatrix} p_{\mathbf{k}}^{11} & p_{\mathbf{k}}^{12} \\ (p_{\mathbf{k}}^{12})^* & -p_{\mathbf{k}}^{11} \end{pmatrix} = \tilde{P}_{\mathbf{k}}, \\ U_{\mathbf{k}}^\dagger L_{\mathbf{k}} U_{\mathbf{k}} = \begin{pmatrix} 0 & 0 \\ 1 & 0 \end{pmatrix} = \tilde{L}_{\mathbf{k}}, \end{cases} \quad (\text{S3.7})$$

where

$$\begin{cases} p_{\mathbf{k}}^{11} = \frac{\epsilon_{\mathbf{k}} \epsilon_{\mathbf{k}}^P + \Delta_{\mathbf{k}}^0 \Delta_{\mathbf{k}}^P}{E_{\mathbf{k}}}, \\ p_{\mathbf{k}}^{12} = -\frac{\epsilon_{\mathbf{k}}^P \Delta_{\mathbf{k}} + i \Delta_{\mathbf{k}}^P \epsilon_{\mathbf{k}}}{E_{\mathbf{k}}} - i \Delta_{\mathbf{k}}^P \frac{\Delta_{\mathbf{k}}^B \Delta_{\mathbf{k}}}{|\Delta_{\mathbf{k}}|^2} \left(1 - \frac{\epsilon_{\mathbf{k}}}{E_{\mathbf{k}}}\right). \end{cases} \quad (\text{S3.8})$$

In addition, using properties of Pauli matrices $\sigma_{x,y,z}$ (note that they are not spin operators), we can rewrite $\tilde{\rho}(\mathbf{k}, t)$, $\tilde{h}(\mathbf{k}, t) = \tilde{M}_{\mathbf{k}} - E_{\text{ac}}(t) \tilde{P}_{\mathbf{k}}$, and $\tilde{P}_{\mathbf{k}}$ as follows:

$$\begin{cases} \tilde{\rho}(\mathbf{k}, t) = \frac{1 + \sum_{\alpha} \tau_{\mathbf{k}}^{\alpha}(t) \sigma_{\alpha}}{2}, \\ \tilde{h}(\mathbf{k}, t)(t) = \sum_{\alpha} h_{\mathbf{k}}^{\alpha}(t) \sigma_{\alpha}, \\ \tilde{P}_{\mathbf{k}}(t) = \sum_{\alpha} p_{\mathbf{k}}^{\alpha} \sigma_{\alpha}, \end{cases} \quad (\text{S3.9})$$

where $\tau_{\mathbf{k}}^{\alpha}(t)$, $h_{\mathbf{k}}^{\alpha}(t)$, and $p_{\mathbf{k}}^{\alpha}$ ($\alpha = x, y, z$) are given by

$$\begin{cases} \tau_{\mathbf{k}}^{\alpha}(t) = \text{Tr}(\tilde{\rho}(\mathbf{k}, t) \sigma_{\alpha}), \\ h_{\mathbf{k}}^{\alpha}(t) = \frac{\text{Tr}(\tilde{h}(\mathbf{k}, t)(t) \sigma_{\alpha})}{2}, \\ p_{\mathbf{k}}^{\alpha} = \frac{\text{Tr}(\tilde{P}_{\mathbf{k}} \sigma_{\alpha})}{2}. \end{cases} \quad (\text{S3.10})$$

Through these instruments, the Lindblad equation (S3.3) for the density matrix $\rho(\mathbf{k}, t)$ is rewritten in the following three-component vector form,

$$\frac{d\boldsymbol{\tau}_{\mathbf{k}}(t)}{dt} = 2\mathbf{h}_{\mathbf{k}}(t) \times \boldsymbol{\tau}_{\mathbf{k}}(t) + \gamma \left(-\boldsymbol{\tau}_{\mathbf{k}}(t) + \frac{1}{2} \begin{pmatrix} \tau_{\mathbf{k}}^x(t) \\ \tau_{\mathbf{k}}^y(t) \\ -2 \end{pmatrix} \right). \quad (\text{S3.11})$$

The initial state is given by

$$\boldsymbol{\tau}_{\mathbf{k}}(t_{\text{ini}}) = \begin{pmatrix} 0 \\ 0 \\ -1 \end{pmatrix}. \quad (\text{S3.12})$$

With $\tau_{\mathbf{k}}^{\alpha}(t)$, the expectation value of the polarization is also rewritten as

$$\begin{aligned} P(t) &= \langle \hat{P} \rangle_t = \frac{1}{N} \sum'_{\mathbf{k}} \text{Tr}(\rho(\mathbf{k}, t) P_{\mathbf{k}}) \\ &= \frac{1}{N} \sum'_{\mathbf{k}} \sum_{\alpha} \tau_{\mathbf{k}}^{\alpha}(t) p_{\mathbf{k}}^{\alpha}. \end{aligned} \quad (\text{S3.13})$$

In our numerical calculation, the total number of unit cells, N , is set to be $N = 160 \times 160$.

S4. RELAXATION-RATE DEPENDENCE OF HHG SPECTRA

As we mentioned in the above section, here we discuss the relaxation-rate dependence of the HHG spectra around the typical value $\gamma = 0.1J$. In Fig. S5, we depicted the numerical results of the spectra under different relaxation rates $\gamma/J = 0.05, 0.1, 0.15$, and 0.2 . Figure S5 shows that smaller γ (longer relaxation time) causes a larger background noise, while the peak positions and intensities of the HHG spectra are robust against moderately change of the value of γ around $\gamma = 0.1J$. Therefore, we can expect that our numerical results with $\gamma = 0.1J$ are basically stable against

a small change of the relaxation rate.

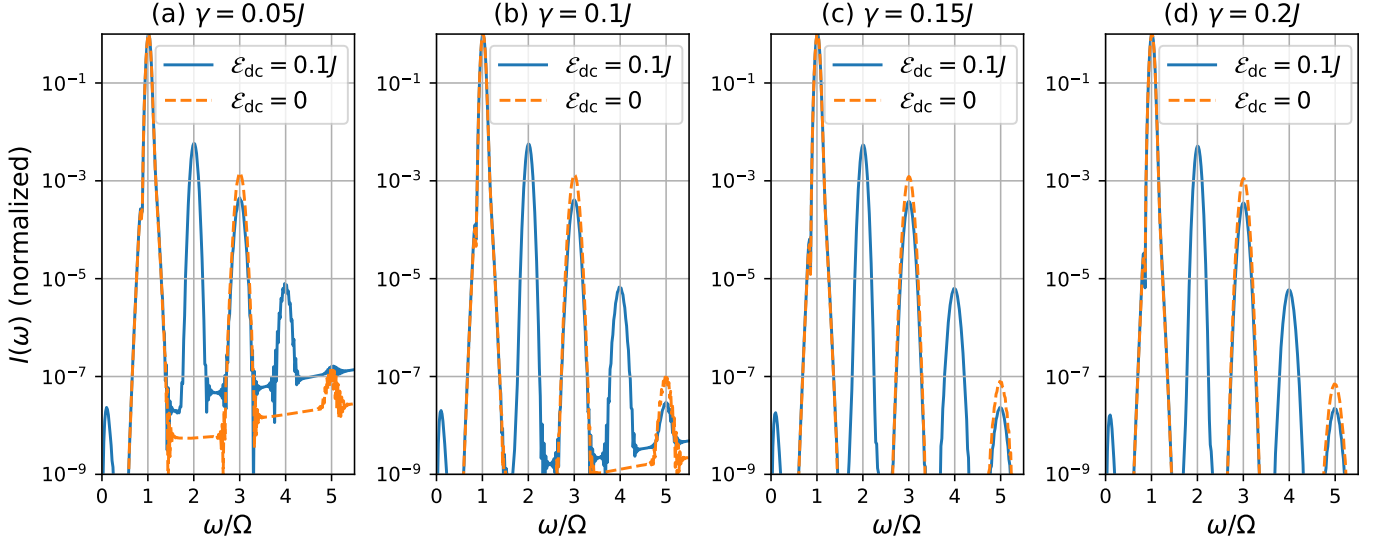


FIG. S5. HHG spectra $I(\omega)$ in the driven ferromagnetic ($J > 0$) Kitaev models under a THz pulse with $\Omega = 2.0J$ and $\mathcal{E}_{ac} = 0.1J$ as a function of ω at $\mathcal{E}_{dc} = 0$ and $0.1J$. Panels (a)–(d) correspond to the results of $\gamma/J = (0.05, 0.1, 0.15, 0.2)$, respectively. $I(\omega)$ is normalized with its maximum value.

S5. LINEAR RESPONSE THEORY FOR POLARIZATION

In this section, we explain the linear response of the polarization \hat{P} to an ac electric field $E_{ac}(t)$. According to linear response theory, the Fourier transform of the linear response of \hat{P} is given by $P(\omega) = \chi_P(\omega)E_{ac}(\omega)$ when the external field $E_{ac}(\omega)$ with frequency ω is sufficiently weak. The susceptibility $\chi_P(\omega)$ is calculated from the imaginary-time two-point function of the polarization with analytic continuation $i\omega_n \rightarrow \omega + i\delta$ (ω_n is Matsubara frequency). Below we show the calculation of $\chi_P(\omega)$. Let us first define the imaginary-time two-point function at finite temperature as

$$\Phi_0(\tau, \tau') = \frac{1}{N} \left\langle T_\tau [\hat{P}(\tau) \hat{P}(\tau')] \right\rangle, \quad (\text{S5.1})$$

where τ is the imaginary time, N is the total number of unit cells, and $T_\tau[\dots]$ means the imaginary-time ordered product. The τ -dependent polarization $\hat{P}(\tau)$ is given by

$$\hat{P}(\tau) = \sum_{\mathbf{k}}' \hat{\mathbf{F}}_{\mathbf{k}}^\dagger(\tau) \tilde{P}_{\mathbf{k}} \hat{\mathbf{F}}_{\mathbf{k}}(\tau), \quad (\text{S5.2})$$

where $\hat{\mathbf{F}}_{\mathbf{k}}(\tau) = \left(\hat{f}_{\mathbf{k}}(\tau) \hat{f}_{-\mathbf{k}}^\dagger(\tau) \right)^\top$ and $\hat{f}_{\mathbf{k}}^\dagger(\tau)$ ($\hat{f}_{\mathbf{k}}(\tau)$) is the fermion creation (annihilation) operator in the imaginary-time Heisenberg representation.

Applying Bloch–De Dominicis theorem to Eq. (S5.1), we obtain

$$\Phi_0(\tau, \tau') = \frac{1}{N} \sum_{\mathbf{k}}' |p_{\mathbf{k}}^{12}|^2 \left(\mathcal{G}^{(0)}(\mathbf{k}, \tau' - \tau) \mathcal{G}^{(0)}(-\mathbf{k}, \tau' - \tau) + \mathcal{G}^{(0)}(\mathbf{k}, \tau - \tau') \mathcal{G}^{(0)}(-\mathbf{k}, \tau - \tau') \right), \quad (\text{S5.3})$$

where $\mathcal{G}^{(0)}(\mathbf{k}, \tau)$ is the imaginary-time Green's function

$$\mathcal{G}^{(0)}(\mathbf{k}, \tau - \tau') = - \left\langle T_\tau [\hat{f}_{\mathbf{k}}(\tau) \hat{f}_{\mathbf{k}}^\dagger(\tau')] \right\rangle. \quad (\text{S5.4})$$

The Fourier transformation of the Green's function and its inverse are respectively represented as

$$\begin{cases} \mathcal{G}^{(0)}(\mathbf{k}, i\omega_n) = \frac{1}{2} \int_{-\beta}^{\beta} e^{i\omega_n \tau} \mathcal{G}^{(0)}(\mathbf{k}, \tau) d\tau, \\ \mathcal{G}^{(0)}(\mathbf{k}, \tau) = k_B T_{\text{em}} \sum_n e^{-i\omega_n \tau} \mathcal{G}^{(0)}(\mathbf{k}, i\omega_n), \end{cases} \quad (\text{S5.5})$$

where k_B and T_{em} are Boltzmann constant and temperature, respectively. $\omega_n = (2n+1)\pi k_B T_{\text{em}}$ ($n \in \mathbb{Z}$) is the fermionic Matsubara frequency. Since the Hamiltonian H_0 is the fermion bilinear form, the Green's function can be easily computed as $\mathcal{G}^{(0)}(\mathbf{k}, i\omega_n) = (i\omega_n - E_{\mathbf{k}})^{-1}$.

Substituting Eq. (S5.5) and $\mathcal{G}^{(0)}(\mathbf{k}, i\omega_n)$ to Eq. (S5.3), we arrive at the Fourier component of $\Phi_0(\tau, \tau')$,

$$\begin{aligned} \Phi_0(i\omega_n) &= \frac{k_B T_{\text{em}}}{N} \sum'_{\mathbf{k}} \sum_m |p_{\mathbf{k}}^{12}|^2 \mathcal{G}^{(0)}(\mathbf{k}, i\omega_m) \left(\mathcal{G}^{(0)}(-\mathbf{k}, i\omega_n - i\omega_m) + \mathcal{G}^{(0)}(-\mathbf{k}, -i\omega_n - i\omega_m) \right) \\ &= \frac{k_B T_{\text{em}}}{N} \sum'_{\mathbf{k}} \sum_m |p_{\mathbf{k}}^{12}|^2 \frac{1}{i\omega_m - E_{\mathbf{k}}} \left(\frac{1}{i\omega_n - i\omega_m - E_{\mathbf{k}}} - \frac{1}{i\omega_n + i\omega_m + E_{\mathbf{k}}} \right). \end{aligned} \quad (\text{S5.6})$$

To compute Eq. (S5.6), we apply the residue theorem and replace the summation of m with complex integrals. We introduce a complex function $F(z) = F_1(z)F_2(z)$, where $F_1(z)$ and $F_2(z)$ are given by

$$\begin{cases} F_1(z) = \frac{1}{e^{\beta z} + 1}, \\ F_2(z) = \frac{1}{z - E_{\mathbf{k}}} \left(\frac{1}{i\omega_n - z - E_{\mathbf{k}}} - \frac{1}{i\omega_n + z + E_{\mathbf{k}}} \right). \end{cases} \quad (\text{S5.7})$$

Figure S6 shows the singularity points of $F(z)$ in the full complex plane of z . $F_1(z)$ has singularity points on the imaginary

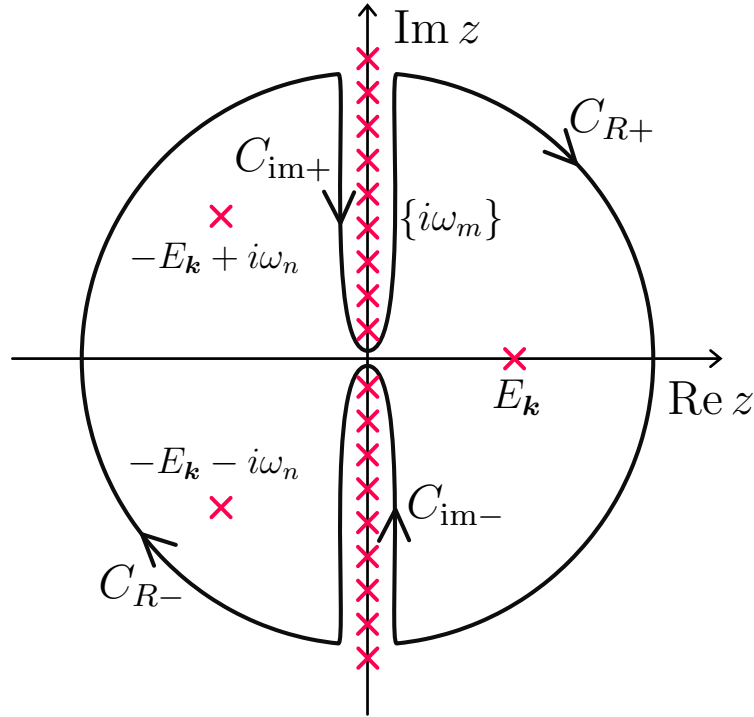


FIG. S6. Integral paths and singularity points of $F(z)$ in the complex plane of z .

axis at $i\omega_m = (2m+1)\pi k_B T_{\text{em}}$ ($n \in \mathbb{Z}$), and $F_2(z)$ has three singularity points at $(z_1, z_2, z_3) = (E_{\mathbf{k}}, -E_{\mathbf{k}} + i\omega_n, -E_{\mathbf{k}} - i\omega_n)$.

From the residue theorem, we find the equality

$$\left(\oint_{C_{\text{im-}}} + \oint_{C_{\text{im+}}} \right) \frac{dz}{2\pi i} F(z) = \sum_m \text{Res } F(z = i\omega_m) = -k_B T_{\text{em}} \sum_m \frac{1}{i\omega_m - E_{\mathbf{k}}} \left(\frac{1}{i\omega_n - i\omega_m - E_{\mathbf{k}}} - \frac{1}{i\omega_n + i\omega_m + E_{\mathbf{k}}} \right), \quad (\text{S5.8})$$

where the paths, $C_{\text{im-}}$ and $C_{\text{im+}}$, respectively surround the imaginary axis in the regime of $\text{Im}z > 0$ and $\text{Im}z < 0$, as shown in Fig. S6. $\text{Res } F(a)$ denotes the residue of $F(z)$ at the point $z = a$. Thus we can rewrite Eq. (S5.6) as

$$\Phi_0(i\omega_n) = -\frac{1}{N} \sum_{\mathbf{k}}' |p_{\mathbf{k}}^{12}|^2 \left(\oint_{C_{\text{im-}}} + \oint_{C_{\text{im+}}} \right) \frac{dz}{2\pi i} F(z). \quad (\text{S5.9})$$

Adding the paths C_{R+} and C_{R-} into $C_{\text{im-}}$ and $C_{\text{im+}}$ (see Fig. S6), we can rewrite Eq. (S5.9) as

$$\Phi_0(i\omega_n) = -\frac{1}{N} \sum_{\mathbf{k}}' |p_{\mathbf{k}}^{12}|^2 \left(\int_{C_{\text{im-}}} + \int_{C_{R-}} + \int_{C_{\text{im+}}} + \int_{C_{R+}} \right) \frac{dz}{2\pi i} F(z). \quad (\text{S5.10})$$

This operation is allowed because of $F(z) \sim z^{-2}$ at $z \rightarrow \infty$. Applying the residue theorem to this closed path, we find the equality

$$\begin{aligned} - \left(\int_{C_{\text{im-}}} + \int_{C_{R-}} + \int_{C_{\text{im+}}} + \int_{C_{R+}} \right) \frac{dz}{2\pi i} F(z) &= \sum_i^3 \text{Res } F(z = z_i) \\ &= \left(\frac{1}{e^{\beta E_{\mathbf{k}}} + 1} + \frac{1}{e^{-\beta E_{\mathbf{k}}} - 1} \right) \left(\frac{1}{i\omega_n - 2E_{\mathbf{k}}} - \frac{1}{i\omega_n + 2E_{\mathbf{k}}} \right). \end{aligned} \quad (\text{S5.11})$$

Therefore, substituting Eq. (S5.11) into Eq. (S5.10), we arrive at

$$\Phi_0(i\omega_n) = \frac{1}{N} \sum_{\mathbf{k}}' |p_{\mathbf{k}}^{12}|^2 \left(\frac{1}{e^{\beta E_{\mathbf{k}}} + 1} + \frac{1}{e^{-\beta E_{\mathbf{k}}} - 1} \right) \left(\frac{1}{i\omega_n - 2E_{\mathbf{k}}} - \frac{1}{i\omega_n + 2E_{\mathbf{k}}} \right). \quad (\text{S5.12})$$

Finally, we perform the analytical continuation $i\omega_n \rightarrow \omega + i\delta$, which changes $\Phi_0(i\omega_n)$ into $\chi(\omega) = \Phi_0(\omega + i\delta)$. The susceptibility is given by

$$\chi(\omega) = \frac{1}{N} \sum_{\mathbf{k}}' |p_{\mathbf{k}}^{12}|^2 \left(\frac{1}{e^{\beta E_{\mathbf{k}}} + 1} + \frac{1}{e^{-\beta E_{\mathbf{k}}} - 1} \right) \left(\frac{1}{\omega - 2E_{\mathbf{k}} + i\delta} - \frac{1}{\omega + 2E_{\mathbf{k}} + i\delta} \right). \quad (\text{S5.13})$$

Taking the zero-temperature limit $\beta \rightarrow \infty$ ($T_{\text{em}} \rightarrow 0$), we obtain

$$\chi_P(\omega) = \lim_{\beta \rightarrow \infty} \chi(\omega) = \frac{1}{N} \sum_{\mathbf{k}}' |p_{\mathbf{k}}^{12}|^2 \left(\frac{1}{\omega + 2E_{\mathbf{k}} + i\delta} - \frac{1}{\omega - 2E_{\mathbf{k}} + i\delta} \right). \quad (\text{S5.14})$$

In our set up of high harmonic generation, we apply a THz laser pulse (not continuous wave) $E_{\text{ac}}(t) = E_{\text{ac}} \cos(\Omega t) f(t)$ with $f(t) = \exp[-2(\ln 2)(t^2/t_{\text{FWHM}}^2)]$ to the Kitaev magnet. Its Fourier component $E_{\text{ac}}(\omega)$ is given by

$$E_{\text{ac}}(\omega) = \frac{E_{\text{ac}}}{2} \sqrt{\frac{\pi}{A}} \left(e^{-\frac{(\omega+\Omega)^2}{4A}} + e^{-\frac{(\omega-\Omega)^2}{4A}} \right), \quad (\text{S5.15})$$

where $A = (2 \log 2)/t_{\text{FWHM}}^2$. In the Green's function, $1/\delta$ is viewed as the life time of the fermions. Therefore, to compare the result of our Lindblad equation with the linear response theory, we set δ to be equal to the relaxation rate γ of the Lindblad equation (S3.3). In Figs. 3 and 4 of the main text, we have depicted both the results of the Lindblad equation and the linear response theory.

S6. SELECTION RULE FOR HHG SPECTRA

In this section, we prove the characteristic selection rule [77–79] of high harmonic generation (HHG) in our Kitaev model. This selection rule becomes exact when incident field is a continuous wave, i.e., $t_{\text{FWHM}} \rightarrow \infty$. Thus, in the following, we assume the continuous wave is applied to the Kitaev model, i.e., envelop function is $f(t) = 1$.

The Hamiltonian for the isotropic Kitaev model without both the dimerization H_{ms} and the three-spin interaction H_{κ} has following symmetry:

$$UH_K U^\dagger = H_K, \quad (\text{S6.1})$$

where the unitary operator U is defined by

$$U = U_{\text{inv}} \Pi_z, \quad (\text{S6.2})$$

with

$$U_{\text{inv}} \sigma_{\mathbf{r}}^\alpha U_{\text{inv}}^\dagger = \sigma_{\mathbf{r}'}^\alpha, \quad (\text{S6.3})$$

$$\Pi_z \sigma_{\mathbf{r}}^\alpha \Pi_z^\dagger = \begin{cases} \sigma_{\mathbf{r}}^y & (\alpha = x), \\ -\sigma_{\mathbf{r}}^x & (\alpha = y), \\ \sigma_{\mathbf{r}}^z & (\alpha = z), \end{cases} \quad (\text{S6.4})$$

where $\mathbf{r}' = (-x, y)^\top$. In the representation of Jordan–Wigner (JW) fermion, this symmetry is expressed as

$$U d_{\mathbf{r}} U^\dagger = d_{\mathbf{r}'}. \quad (\text{S6.5})$$

Through Fourier transformation, Eq. (S6.5) is rewritten as

$$U \tilde{d}_{\mathbf{k}} U^\dagger = \tilde{d}_{\mathbf{k}'}, \quad (\text{S6.6})$$

where $\mathbf{k}' = (-k_x, k_y)^\top$. Thus, the Hamiltonian,

$$H_K = \sum_{\mathbf{k}}' \hat{h}(\mathbf{k}) = \sum_{\mathbf{k}}' \left[\epsilon_{\mathbf{k}}^{\text{iso}} \tilde{d}_{\mathbf{k}}^\dagger \tilde{d}_{\mathbf{k}} - \epsilon_{\mathbf{k}}^{\text{iso}} \tilde{d}_{-\mathbf{k}} \tilde{d}_{-\mathbf{k}}^\dagger - i \Delta_{\mathbf{k}}^{\text{iso}} \left(\tilde{d}_{\mathbf{k}}^\dagger \tilde{d}_{-\mathbf{k}}^\dagger - \tilde{d}_{-\mathbf{k}} \tilde{d}_{\mathbf{k}} \right) \right], \quad (\text{S6.7})$$

satisfies the following transformation:

$$U \hat{h}(\mathbf{k}) U^\dagger = \hat{h}(\mathbf{k}'). \quad (\text{S6.8})$$

Following the similar argument, we find that the polarization $\hat{P} = \sum_{\mathbf{k}}' \hat{p}(\mathbf{k})$ obeys

$$U \hat{p}(\mathbf{k}) U^\dagger = -\hat{p}(\mathbf{k}'). \quad (\text{S6.9})$$

Two equations (S6.8) and (S6.9) tell us that the driven Kitaev Hamiltonian $H_K - E_{\text{ac}}(t) \hat{P} = \sum_{\mathbf{k}}' (\hat{h}(\mathbf{k}) - E_{\text{ac}}(t) \hat{p}(\mathbf{k}))$ follows

$$U \hat{h}(\mathbf{k}, t) U^\dagger = \hat{h}(\mathbf{k}', t + T/2), \quad (\text{S6.10})$$

where $\hat{h}(\mathbf{k}, t) = \hat{h}(\mathbf{k}) - E_{\text{ac}}(t) \hat{p}(\mathbf{k})$.

Next, we consider a dynamical symmetry of the density matrix. We symbolically represent the quantum master equation (S6.11) by using the Liouvillian super-operator $\mathcal{L}_{\mathbf{k}}(t)$:

$$\frac{d}{dt} \hat{\rho}(\mathbf{k}, t) = \mathcal{L}_{\mathbf{k}}(t) \hat{\rho}(\mathbf{k}, t). \quad (\text{S6.11})$$

Our Lindblad operator satisfies

$$U L_{\mathbf{k}} U^\dagger = e^{i\theta_{\mathbf{k}}} L_{\mathbf{k}'} \quad (\theta_{\mathbf{k}} \in \mathbb{R}). \quad (\text{S6.12})$$

From two equations (S6.12) and (S6.10), we obtain

$$\frac{d}{dt}\hat{\rho}(\mathbf{k}', t + T/2) = \mathcal{L}_{\mathbf{k}'}\hat{\rho}(\mathbf{k}', t + T/2) = U\mathcal{L}_{\mathbf{k}}U^\dagger\hat{\rho}(\mathbf{k}', t + T/2), \quad (\text{S6.13})$$

hence

$$\frac{d}{dt}U^\dagger\hat{\rho}(\mathbf{k}', t + T/2)U = \mathcal{L}_{\mathbf{k}}U^\dagger\hat{\rho}(\mathbf{k}', t + T/2)U. \quad (\text{S6.14})$$

Comparing Eqs. (S6.11) and (S6.14), we find the equality

$$U\hat{\rho}(\mathbf{k}, t)U^\dagger = \hat{\rho}(\mathbf{k}', t + T/2). \quad (\text{S6.15})$$

Using this dynamical symmetry of the density matrix, we compute the Fourier component of the polarization as

$$\begin{aligned} p(\mathbf{k}, t) &= \langle \hat{p}(\mathbf{k}) \rangle_t = \text{Tr} [\hat{\rho}(\mathbf{k}, t)\hat{p}(\mathbf{k})] \\ &= -\text{Tr} [\hat{\rho}(\mathbf{k}', t + T/2)\hat{p}(\mathbf{k}')] \\ &= -p(\mathbf{k}', t + T/2). \end{aligned} \quad (\text{S6.16})$$

This leads to

$$\begin{aligned} P(t) &= \frac{1}{N} \sum'_{\mathbf{k}} p(\mathbf{k}, t) \\ &= -\frac{1}{N} \sum'_{\mathbf{k}} p(\mathbf{k}', t + T/2) \\ &= -\frac{1}{N} \sum'_{\mathbf{k}} p(\mathbf{k}, t + T/2) \\ &= -P(t + T/2), \end{aligned} \quad (\text{S6.17})$$

where we have used $p(\mathbf{k}, t) = p(-\mathbf{k}, t)$ in the third line. This result directly leads to the absence of the even-order HHG spectra. Namely, from Eq. (S6.17), the n -th harmonic polarization $P(n\Omega)$ is calculated as

$$\begin{aligned} P(n\Omega) &= \int_0^T \frac{dt}{T} P(t) e^{in\Omega t} \\ &= \int_{-T/2}^{T/2} \frac{dt}{T} P(t + T/2) e^{in\Omega(t+T/2)} \\ &= -e^{in\Omega \frac{T}{2}} \int_{-T/2}^{T/2} \frac{dt}{T} P(t) e^{in\Omega t} \\ &= -e^{in\pi} P(n\Omega), \end{aligned} \quad (\text{S6.18})$$

which means

$$P(2m\Omega) = 0 \quad (m \in \mathbb{Z}). \quad (\text{S6.19})$$

That is, we find that the even-order HHGs are all absent in the system of $H_K - E_{ac}(t)\hat{P}$. Our numerical results are consistent with this symmetry argument at $E_{dc} = 0$. See Fig. 2(a) of the main text.

Applying a DC electric field E_{dc} to the system, the Hamiltonian is modified to

$$H(t) = H_0 - E_{dc}\hat{P} - E_{ac}(t)\hat{P}. \quad (\text{S6.20})$$

In this case, the dynamical symmetry is broken and

$$UH(t)U^\dagger \neq H(t + T/2). \quad (\text{S6.21})$$

Therefore, in a dimerized (i.e., anisotropic) Kitaev model, even-order polarizations $P(2m\Omega)$ are generally not

prohibited. Our numerical calculation shows that a finite $P(2m\Omega)$ emerges if we introduce $E_{\text{dc}} \neq 0$.

Next, we also consider the isotropic Kitaev model with a three-spin interaction term, $H_K + H_\kappa$ with a finite κ . In this case, let us introduce the time-reversal operator \hat{V} , which satisfies

$$\hat{V}\sigma_r^\alpha\hat{V}^\dagger = -\sigma_r^\alpha \quad (\alpha = x, y, z). \quad (\text{S6.22})$$

Combining \hat{U} and \hat{V} , we can find that the Hamiltonian $H_K + H_\kappa$ has following symmetry:

$$\hat{V}\hat{U}(H_K + H_\kappa)(\hat{V}\hat{U})^\dagger = H_K + H_\kappa. \quad (\text{S6.23})$$

Replacing \hat{U} with $\hat{V}\hat{U}$ in the above dynamical-symmetry argument about H_K , we can show that even-order HHGs all disappear in the system of $H_K + H_\kappa - E_{\text{ac}}(t)\hat{P}$.

S7. MAGNETIC ANISOTROPY DEPENDENCE OF EVEN-ORDER HARMONICS

As discussed in the main text and the above section, we can apply the dynamical symmetry and selection rule in a wide class of Kitaev models with various perturbations. In the main text, we have focused on the isotropic point ($J_{x,y,z} = J$) while Kitaev candidates sometimes possess a magnetic anisotropy, i.e., inequivalence of J_x , J_y , and J_z . Here, we study the even-order harmonics in an anisotropic Kitaev model without dc electric field. The argument in the above section tells us that the dynamical symmetry survives for $J_z \neq J_x = J_y$, while it breaks down for $J_x \neq J_y$. Therefore, the anisotropic Kitaev models with $J_x \neq J_y$ are expected to possess a finite intensity of even-order harmonics. Using the master equation, we numerically calculate the anisotropy dependence of the even-order harmonics in the anisotropic Kitaev models and the result is given in Fig. S7. This figure clearly indicates that a finite anisotropy ($J_x \neq J_y$) indeed induces peaks of even-order harmonics (SHG and FHG).

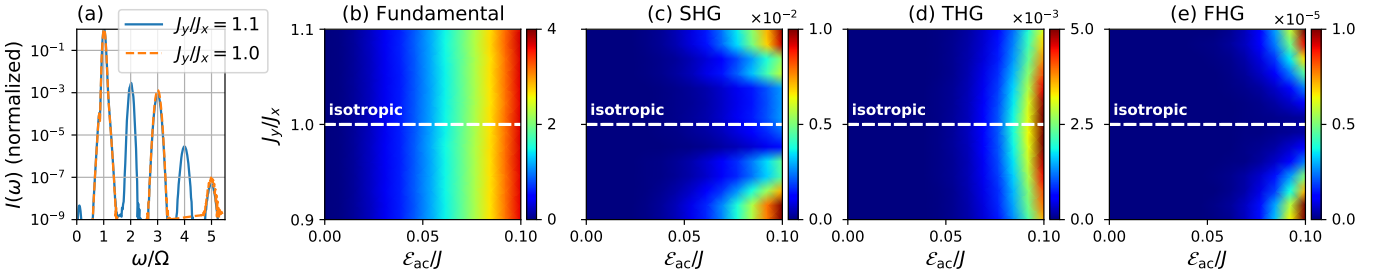


FIG. S7. HHG spectra $I(\omega)$ in anisotropic ferromagnetic ($J_{x,y,z} > 0$) Kitaev models under a THz pulse of $\Omega = 2.0J_x$. (a) $I(\omega)$ as a function of ω at $J_y/J_x = 1$ and 1.1 under the irradiation of $\mathcal{E}_{\text{ac}} = 0.1J_x$. $I(\omega)$ is normalized with its maximum value. (b)–(e) $(\mathcal{E}_{\text{ac}}, J_y/J_x)$ dependence of fundamental harmonic [$I(\Omega)$], SHG [$I(2\Omega)$], THG [$I(3\Omega)$], and FHG [$I(4\Omega)$] spectra. The unit of intensity is chosen as $I(\Omega)$ at $\mathcal{E}_{\text{ac}} = 0.05J_x$ and $J_y/J_x = 1$. The other parameters are set to be $J_z = J_x$, $\gamma = 0.1J_x$, and $E_{\text{dc}} = 0$.

S8. κ DEPENDENCE OF DENSITY OF STATES

In the main text, we have discussed the κ dependence of the density of state (DoS) $\mathcal{D}(\omega)$ of fermions $f_{\mathbf{k}}$ in the antiferromagnetic Kitaev model with $J < 0$. Physically, κ is proportional to the cubic of external magnetic field \mathbf{B} . Therefore, the κ -dependent DoS tells us its $|\mathbf{B}|$ dependence. In this section, we shortly discuss the shape of $\mathcal{D}(\omega)$ as a function of κ in more detail. Figures S8 and S9 depict DoSs $\mathcal{D}(\omega)$ for different value of κ . Panels (a)–(e) are the result for the isotropic Kitaev models with $E_{\text{dc}} = 0$, while panels (f)–(j) are those of the dimerized model with $E_{\text{dc}}\eta_{\text{ms}} = 0.1|J|$.

In Fig. S8, we focus on the weak κ region of $\kappa \lesssim 0.2|J|$, which correspond to the regime of weak dc magnetic fields. The fermion mass gap Δ_κ monotonically increases with the growth of $\kappa \sim |\mathbf{B}|^3$. Panels (a)–(e) show that when the mass gap Δ_κ increases for $E_{\text{dc}} = 0$, the highest value (peak height) of $\mathcal{D}(\Omega_0)$ i.e., $\mathcal{D}(\Omega_0 \sim 2|J|)$, also grows up. For $E_{\text{dc}} \neq 0$, the peak of $\mathcal{D}(\Omega_0)$ is split into three peaks, as shown in panels (f)–(j). However, a similar κ dependence remains, i.e., the height of three peaks increases with the growth of Δ_κ . We note that the peak frequency $\Omega_0 \sim 2|J|$ is almost unchanged in this weak κ regime.

On the other hand, Fig. S9 tells us that different behavior of the gap Δ_κ and peak frequency appears in the strong κ regime of $\kappa \gtrsim 0.2|J|$. Figure S9 shows that the mass gap Δ_κ is almost fixed at $\Delta_\kappa \sim 2|J|$, while the peak position Ω_0 of $D(\omega)$ almost linearly increases with $\kappa \sim |\mathbf{B}|^3$ for both $E_{\text{dc}} = 0$ and $E_{\text{dc}} \neq 0$.

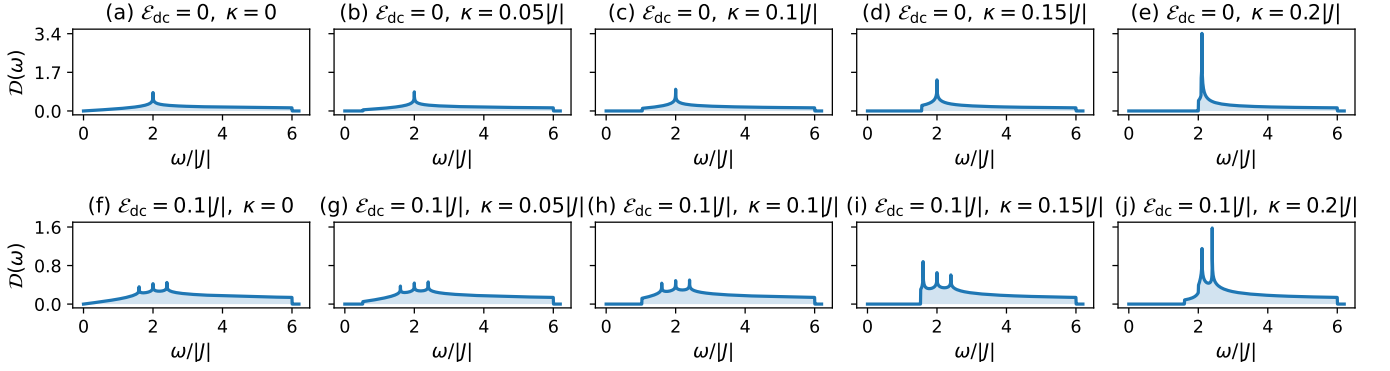


FIG. S8. κ dependences of DoSs in the antiferromagnetic ($J < 0$) Kitaev models at $\kappa/|J| = (0, 0.05, 0.1, 0.15, 0.2)$ with (a-e) $\mathcal{E}_{\text{dc}} = 0$ and (f-j) $\mathcal{E}_{\text{dc}} = 0.1|J|$.

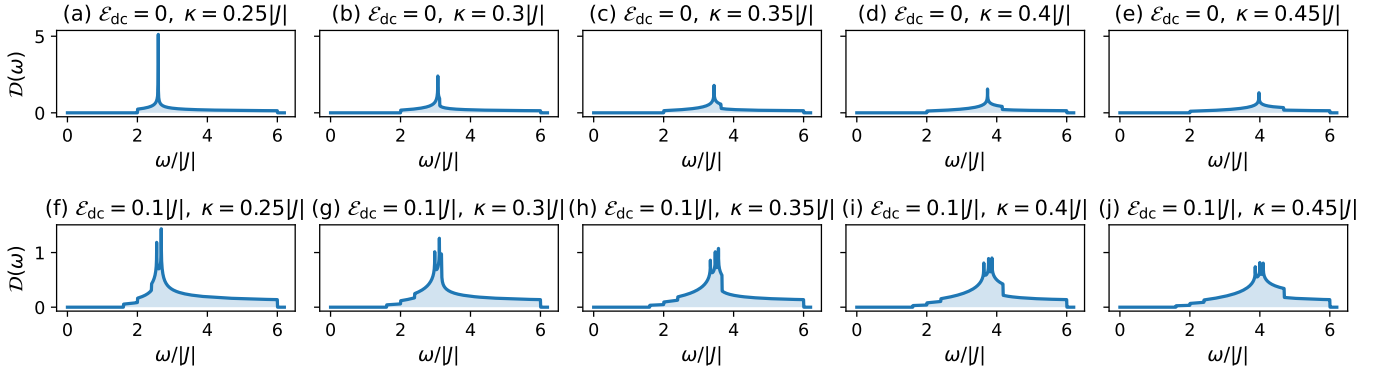


FIG. S9. κ dependences of DoSs in the antiferromagnetic ($J < 0$) Kitaev models at $\kappa/|J| = (0.25, 0.3, 0.35, 0.4, 0.45)$ with (a-e) $\mathcal{E}_{\text{dc}} = 0$ and (f-j) $\mathcal{E}_{\text{dc}} = 0.1|J|$.

S9. HHG IN ANTIFERROMAGNETIC KITAEV MODEL WITH DC ELECTRIC FIELD

In the main text, we have shown some characteristic features of the dc-electric-field dependence of HHG in the ferromagnetic Kitaev model. In this section, we discuss the dc-electric-field E_{dc} and laser-frequency Ω dependences of HHG in antiferromagnetic Kitaev model ($J < 0$).

Figure S10 represents the $(E_{\text{ac}}, E_{\text{dc}})$ dependences of fundamental harmonic, SHG, THG, and FHG in the antiferromagnetic Kitaev models. From the panels (b) and (d), we see that even-order harmonics (SHG and FHG) appear only when a finite dc field E_{dc} is introduced to the system. This is owing to the fact that there is the same dynamical symmetry as the ferromagnetic Kitaev model [Sec. S6] for the case of zero dc electric field $E_{\text{dc}} = 0$. We have verified that the $(E_{\text{ac}}, E_{\text{dc}})$ dependences of HHG in the antiferromagnetic case are very similar to those in the ferromagnetic one.

Figure S11 shows a fundamental harmonic, SHG, and THG of the same antiferromagnetic Kitaev models in the space (E_{ac}, Ω) . We find broad peaks in all of $I(\Omega)$, $I(2\Omega)$, and $I(3\Omega)$. The peaks of $I(2\Omega)$ and $I(3\Omega)$ appear around $\Omega = \Omega_{\text{peak}}/2$ and $\Omega_{\text{peak}}/3$, respectively. This is the natural result from the view of the perturbation theory with respect to the laser intensity. These results are also similar to those of the ferromagnetic model.

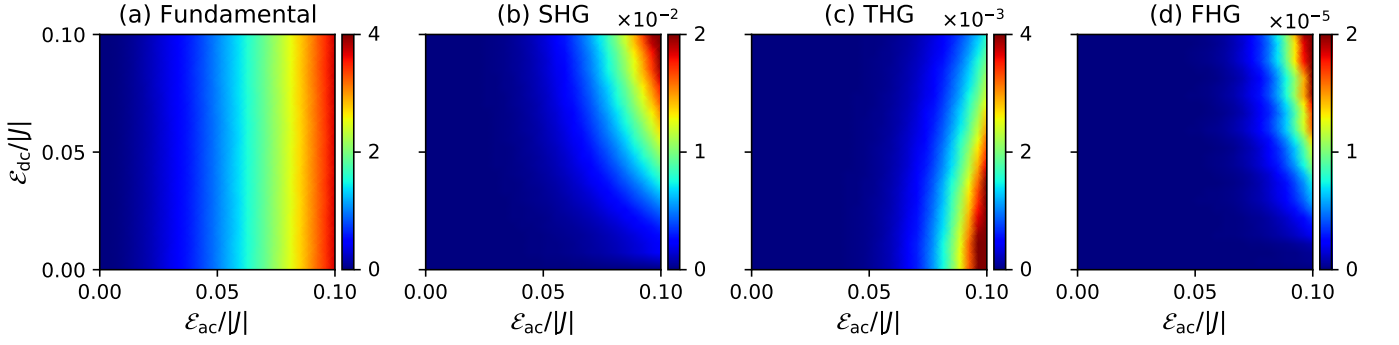


FIG. S10. Intensities of (a) fundamental harmonic [$I(\Omega)$], (b) SHG [$I(2\Omega)$], (c) THG [$I(3\Omega)$], and (d) FHG [$I(4\Omega)$] in the antiferromagnetic ($J < 0$) Kitaev models driven by THz laser of $\Omega = 2.0|J|$ in the space $(\mathcal{E}_{ac}, \mathcal{E}_{dc})$. The unit of intensity is chosen as $I(\Omega)$ at $\mathcal{E}_{ac} = 0.05|J|$ and $\mathcal{E}_{dc} = 0.05|J|$. The relaxation rate is set to be $\gamma = 0.1|J|$.

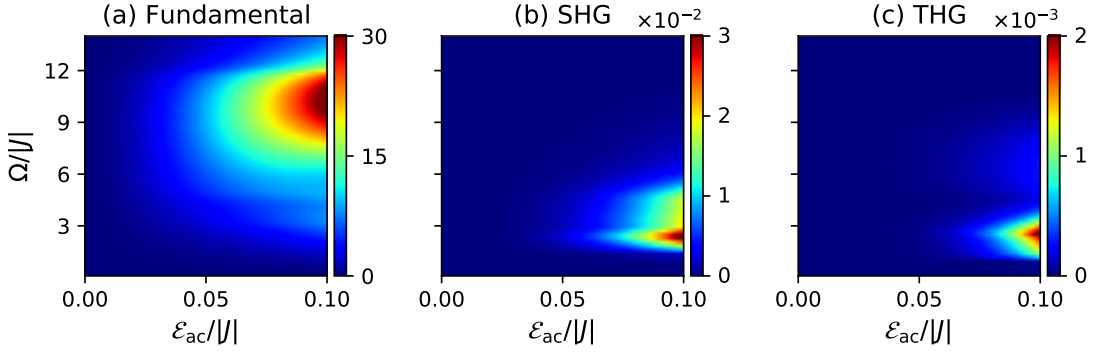


FIG. S11. Intensities of (a) fundamental harmonic [$I(\Omega)$], (b) SHG [$I(2\Omega)$], and (c) THG [$I(3\Omega)$] in the driven antiferromagnetic ($J < 0$) Kitaev models with laser of $\Omega = 2|J|$ and $\mathcal{E}_{dc} = 0.1|J|$ in the space $(\mathcal{E}_{ac}, \Omega)$. The unit of intensity is chosen as $I(\Omega)$ at $\mathcal{E}_{ac} = 0.05|J|$ and $\Omega = 2.0|J|$. The relaxation rate is $\gamma = 0.1|J|$.

S10. HHG IN KITAEV HONEYCOMB MODEL WITH DC MAGNETIC FIELD

In this section, we discuss effect of a dc magnetic field on the HHG of the Kitaev model. In our present study, the effect of dc magnetic field is taken in the κ term H_κ of the three-spin interaction. As we already mentioned, the microscopic origin of the coupling constant κ is a usual Zeeman coupling with dc magnetic field \mathbf{B} and the relation $\kappa \sim |\mathbf{B}|^3$ is hold. As we mentioned in the main text, when we apply a dc magnetic field \mathbf{B} to a static Kitaev model, the spin liquid state suddenly changes into a ferromagnetic phase for ferromagnetic case ($J > 0$). On the other hand, the spin liquid phase is relatively stable against \mathbf{B} in the antiferromagnetic model with $J < 0$. Therefore, we note that the antiferromagnetic Kitaev model is more realistic if we take into account the effect of \mathbf{B} by introducing the κ term.

First, we discuss the (E_{ac}, κ) dependences of fundamental harmonic, SHG, THG, and FHG in ferromagnetic ($J > 0$) [Figs. S12(a-d)] and antiferromagnetic ($J < 0$) [Figs. S13(a-d)] Kitaev models. Panels (e-h) respectively show the κ dependences of the fermion DoSs $\mathcal{D}(\omega)$ corresponding to panels (a-d). The intensity peaks of the fundamental harmonic (SHG) appear when the laser frequency Ω approaches the points where DoS $\mathcal{D}(\Omega/2)$ ($\mathcal{D}(\Omega)$) take the highest value. This is natural from the perturbative picture of the laser effect. However, the nontrivial peak distributions occur in the THG and FHG, and they cannot be explained from the simple perturbation theory. These peaks may be attributed to not only inter-band fermion-pair transition process but also the intra-band dynamics, which will be explained in Sec. S11. We also find that there is no significant difference between the ferromagnetic and antiferromagnetic cases.

Next, in Fig. S14, we depict the (κ, Ω) dependences of fundamental harmonic, SHG, and THG in the antiferromagnetic Kitaev models ($J < 0$) under a strong laser pulse with $\mathcal{E}_{ac} = 0.1|J|$. Figures S14(a) and S14(b) are also depicted in Fig. 4 of the main text. As we discussed in the main text, the frequency Ω at the broad peak position monotonically increases in an almost κ -linear fashion for fundamental harmonic $I(\Omega)$ in the case of $\kappa \gtrsim 0.2|J|$. This is because the peak position Ω_0 of $\mathcal{D}(\Omega)$ almost linearly increases with κ for $\kappa \gtrsim 0.2|J|$. We give Fig. S15 to

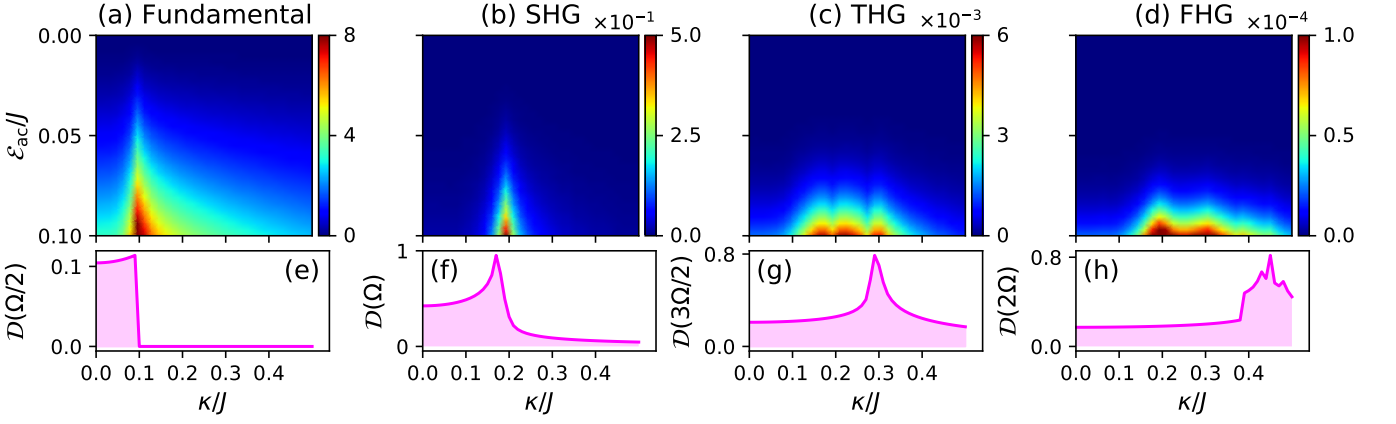


FIG. S12. Intensities of (a) fundamental harmonic $[I(\Omega)]$, (b) SHG $[I(2\Omega)]$, (c) THG $[I(3\Omega)]$, and (d) FHG $[I(4\Omega)]$ in the slightly-anisotropic ($\mathcal{E}_{dc} = 0.1J$) ferromagnetic ($J > 0$) Kitaev models driven by laser pulse of $\Omega = 2J$ in the space $(\mathcal{E}_{ac}, \kappa)$. (e–h) DoS $\mathcal{D}(\omega)$ as a function of κ : (e)–(h) respectively correspond to panels (a)–(d). The unit of intensity is chosen as $I(\Omega)$ at $\mathcal{E}_{ac} = 0.05J$ and $\kappa = 0.05J$. The relaxation rate is set to be $\gamma = 0.1J$.

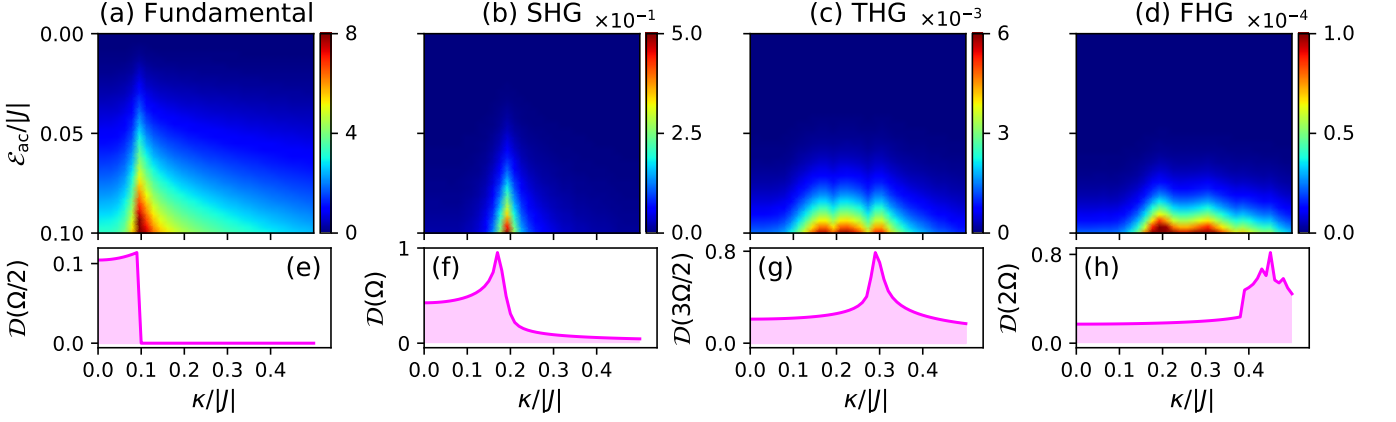


FIG. S13. Intensities of (a) fundamental harmonic $[I(\Omega)]$, (b) SHG $[I(2\Omega)]$, (c) THG $[I(3\Omega)]$, and (d) FHG $[I(4\Omega)]$ in the slightly-anisotropic ($\mathcal{E}_{dc} = 0.1|J|$) antiferromagnetic ($J < 0$) Kitaev models driven by laser pulse of $\Omega = 2|J|$ in the space $(\mathcal{E}_{ac}, \kappa)$. (e–h) DoS $\mathcal{D}(\omega)$ as a function of κ : (e)–(h) respectively correspond to panels (a)–(d). The unit of intensity is chosen as $I(\Omega)$ at $\mathcal{E}_{ac} = 0.05|J|$ and $\kappa = 0.05|J|$. The relaxation rate is set to be $\gamma = 0.1|J|$.

more clearly show this relation among κ , the peak position Ω_0 of the DoS, and that of the fundamental harmonic $I(\Omega)$ (see also Fig. S9). One can verify that the peak position of $I(\Omega)$ indeed coincides with that of the DoS, Ω_0 for $\kappa \gtrsim 0.2|J|$. Since $\kappa \sim |\mathbf{B}|^3$, the \mathbf{B} -cube dependent peak frequency is specific for the Kitaev model. In usual magnets, the magnetic-resonance frequency Ω is proportional to $|\mathbf{B}|$. The peak frequency of $I(2\Omega)$ is almost half of Ω_{peak} of $I(\Omega)$ as shown in Fig. S14(b), and this is a natural result from the perturbative viewpoint. However, the nontrivial peak occurs in the THG and this peak may be explained by the non-perturbative intra-band dynamics. This intra-band dynamics will be discussed in Sec. S11.

In the case of a weak pulse ($\mathcal{E}_{ac} = 10^{-3}|J|$), we also observe a sharp peak of $I(\Omega)$ at Ω_{peak} in Fig. S16. This result indicates that, even in the linear response regime, the fundamental harmonic shows characteristics of the Kitaev QSL for $\kappa \gtrsim 0.2|J|$. $I(\Omega)$ driven by intense pulses with a finite magnetic field tells us the peak position of the DoS Ω_0 , which is half as large as Ω_{peak} .

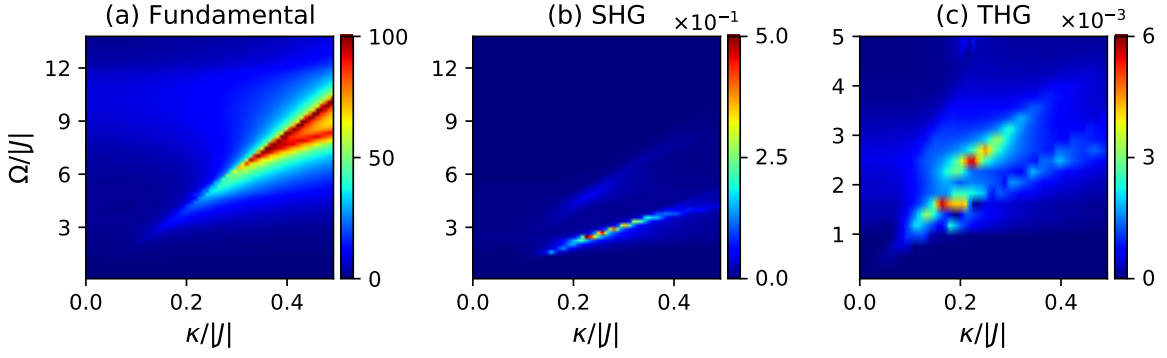


FIG. S14. Intensities of (a) fundamental harmonic $[I(\Omega)]$, (b) SHG $[I(2\Omega)]$, and (c) THG $[I(3\Omega)]$ in the slightly-anisotropic ($\mathcal{E}_{\text{dc}} = 0.1|J|$) antiferromagnetic ($J < 0$) Kitaev models driven by laser pulse of intensity $\mathcal{E}_{\text{ac}} = 0.1|J|$ in the space (κ, Ω) . The unit of intensity is chosen as $I(\Omega)$ at $\Omega = 2.0|J|$ and $\kappa = 0.05|J|$. The relaxation rate is set to be $\gamma = 0.1|J|$.

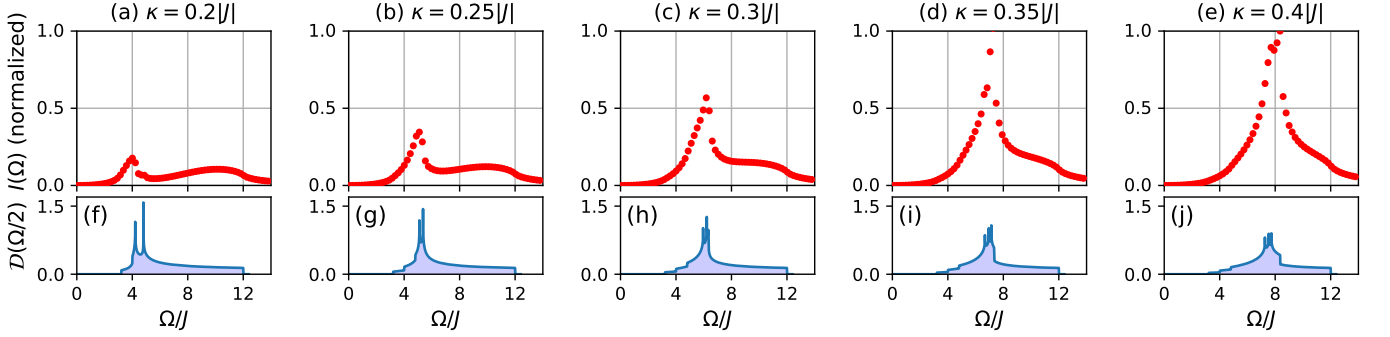


FIG. S15. (a)–(e) $I(\Omega)$ of the antiferromagnetic ($J < 0$) Kitaev models with $\mathcal{E}_{\text{dc}} = 0.1|J|$ and $\mathcal{E}_{\text{ac}} = 0.1|J|$ at (a) $\kappa/|J| = 0.2$, (b) 0.25, (c) 0.3, (d) 0.35, and (e) 0.4. $I(\Omega)$ in panels (a)–(e) are normalized with the maximum value in the panel (e). Panels (f)–(j) show DoSs of fermions corresponding to the cases (a)–(e), respectively.

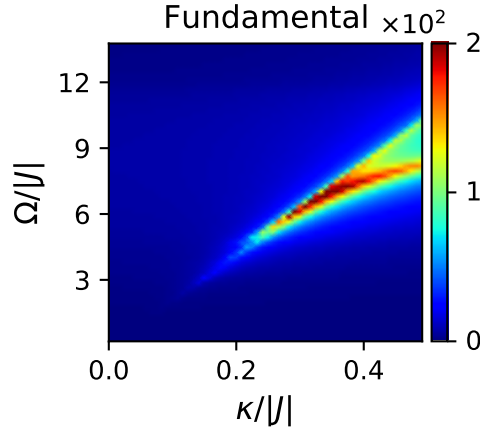


FIG. S16. Intensity of fundamental harmonic $[I(\Omega)]$ in the slightly-anisotropic ($\mathcal{E}_{\text{ac}} = 0.1|J|$) antiferromagnetic ($J < 0$) Kitaev models driven by laser pulse of intensity $\mathcal{E}_{\text{ac}} = 10^{-3}|J|$ in the space (κ, Ω) . The unit of intensity is chosen as $I(\Omega)$ at $\Omega = 2.0|J|$ and $\kappa = 0.05|J|$. The relaxation rate is set to be $\gamma = 0.1|J|$.

S11. INTRA- AND INTER-BAND DYNAMICS IN DRIVEN KITAEV MODEL

In this section, we consider the laser-induced dynamics in the driven Kitaev model from the microscopic viewpoint of the fermion band structure. If the applied THz laser is sufficiently weak, the vacuum state is weakly perturbed by photons and only the dynamics including a few fermions is important. In this case, the resonant-like process creating

fermion pairs with \mathbf{k} and $-\mathbf{k}$ is dominant. Namely, when the fermion-pair excitation energy coincides with the photon energy $\hbar\Omega$, the fermion pairs are strongly created. This may be called the inter-band dynamics. However, if the laser pulse becomes strong, the situation is expected to be different. In this case, in addition to the resonant pair creations and their relaxation, the intra-band dynamics processes may also contribute to HHG due to the nonlinear optical (multiple photon) effect. We discuss this expectation from the numerical calculation below.

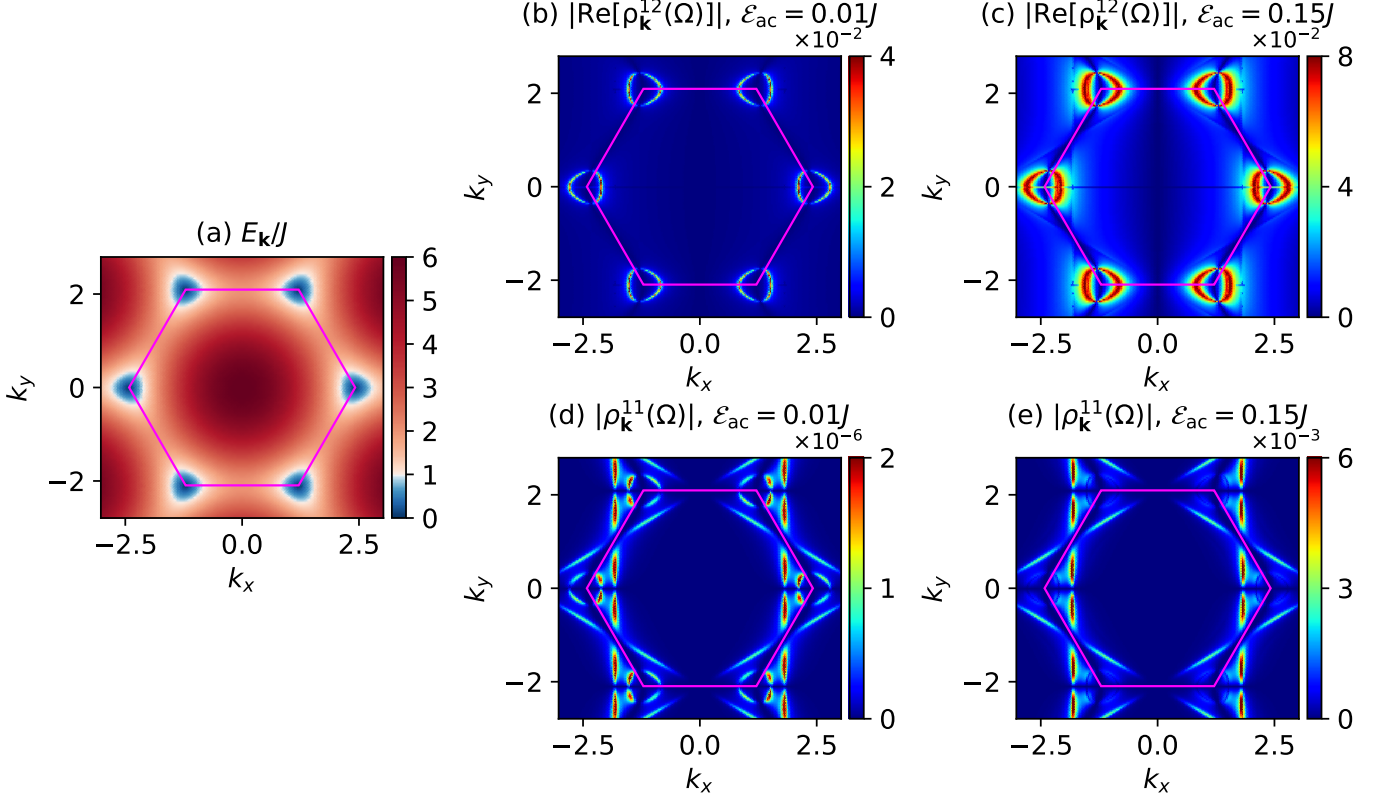


FIG. S17. (a) Fermion band structure of the isotropic antiferromagnetic ($J < 0$) Kitaev model H_K with $\mathcal{E}_{dc} = \kappa = 0$. The white areas around K and K' points in Brillouin zone correspond to the excitation energy J . (b),(c) Fourier components of the off-diagonal elements $|\text{Re}[\rho_{\mathbf{k}}^{12}(\Omega)]|$ for the Kitaev model driven by THz laser with frequency $\Omega = 2J$ at (b) $\mathcal{E}_{ac} = 10^{-2}J$ and (c) $\mathcal{E}_{ac} = 0.15J$. (d),(e) Diagonal parts $|\rho_{\mathbf{k}}^{11}(\Omega)|$ for the same driven Kitaev model at (d) $\mathcal{E}_{ac} = 10^{-2}J$ and (e) $\mathcal{E}_{ac} = 0.15J$. We set the parameters of the Kitaev model to be $\mathcal{E}_{dc} = \kappa = 0$, and the relaxation rate is set to be $\gamma = 0.1J$.

We have defined the 2×2 density matrix $\rho_{\mathbf{k}}$ with the bases of the ground state $|g_{\mathbf{k}}\rangle$ and the excited one $|e_{\mathbf{k}}\rangle$. Therefore, the inter-band dynamics is reflected in the off-diagonal elements $\rho_{\mathbf{k}}^{12} = (\rho_{\mathbf{k}}^{21})^*$, while the intra-band dynamics can be observed in the diagonal part $\rho_{\mathbf{k}}^{11} = 1 - \rho_{\mathbf{k}}^{22}$. We calculate the laser-driven dynamics of the density matrix $\rho_{\mathbf{k}}$ in the full Brillouin zone. Figure S17 shows the Fourier component of $|\rho_{\mathbf{k}}^{11}|$ and $|\text{Re}[\rho_{\mathbf{k}}^{12}]|$ for the Kitaev model under the laser with $\Omega = 2J$. As the reference, we show the Fermion energy band structure in Fig. S17(a), in which the regime of $\Omega/2 = E_{\mathbf{k}}/J = 1$ is depicted by white color. Figures S17(b) and S17(c) represent the Fourier components of the off-diagonal elements $|\text{Re}[\rho_{\mathbf{k}}^{12}(\Omega)]|$ for weak ($\mathcal{E}_{ac} = 10^{-2}J$) and strong ($\mathcal{E}_{ac} = 0.15J$) laser intensities, respectively. Similarly, Figs. S17(d) and S17(e) respectively show the off-diagonal components $|\rho_{\mathbf{k}}^{11}(\Omega)|$ for weak and strong lasers. From Figs. S17(a)–S17(c), we see that the inter-band dynamics (i.e., $|\text{Re}[\rho_{\mathbf{k}}^{12}(\Omega)]|$) are much active around the regime of $\Omega/2 = E_{\mathbf{k}}/J = 1$ irrespectively of the strength of laser. It indicates that (as expected) the resonant-like dynamics is always dominant in HHG of the Kitaev model.

For weak laser pulse, Figs. S17(b) and S17(d) show that the ratio $C(\mathcal{E}_{ac} = 10^{-2}J) = \max[|\rho_{\mathbf{k}}^{11}(\Omega)|] / \max[|\text{Re}[\rho_{\mathbf{k}}^{12}(\Omega)]|] \sim 10^{-4}$, which indicates that the resonant-like process of the off-diagonal dynamics is dominant in the HHG. (Here, $\max[\dots]$ means the maximum value in the Brillouin zone.) On the other hand, Figs. S17(c) and S17(e) show that the ratio increases as $C(\mathcal{E}_{ac} = 0.15J) \sim 10^{-1}$ for the strong THz pulse. This means that the intra-band transition process becomes more important than that for a weak THz pulse. The increase of $|\rho_{\mathbf{k}}^{11}(\Omega)|$ is thereby viewed as a signature of nonlinear optical effects.

From Figs. S17(b)–(e), we also find that the regime with high value of $|\text{Re}[\rho_{\mathbf{k}}^{12}(\Omega)]|$ does not overlap well that with

intense $|\rho_{\mathbf{k}}^{11}(\Omega)|$, namely, the active areas of $|\text{Re}[\rho_{\mathbf{k}}^{12}(\Omega)]|$ and $|\rho_{\mathbf{k}}^{11}(\Omega)|$ are independently of each other.

S12. NONLINEARITY OF HHG AND REQUIRED LASER INTENSITY

In this section, we discuss the crossover from linear to nonlinear responses, and estimate the laser intensity required to observe HHG in the experiment.

First, we consider the crossover. Figure S18 shows the low-order harmonics of the polarization $P(n\Omega)$ ($n = 1, 2, 3, 4$) versus laser intensity in the ferromagnetic ($J > 0$) Kitaev model with $\mathcal{E}_{\text{dc}} = 0.1J$ under THz laser with frequency $\Omega = 2J$. When the laser intensity is sufficiently weak, $P(n\Omega)$ increase with the growth of laser intensity \mathcal{E}_{ac} . We observe the relation $P(n\Omega) \propto \mathcal{E}_{\text{ac}}^n$. This indicates that the perturbation theory is reliable in this weak laser regime. On the other hand, as the laser intensity is increased, the power-law relation is gradually violated, and $P(n\Omega)$ becomes smaller than the fitting curve of $P(n\Omega) \propto \mathcal{E}_{\text{ac}}^n$. This violation stems from multiple photon processes beyond the leading contribution of the perturbation theory. Figure S18 shows that the deviation from the fitting curve starts when the laser intensity becomes beyond $\mathcal{E}_{\text{ac}}/J > 0.1$. Our approach based on Lindblad equation can capture both perturbative and non-perturbative regimes.

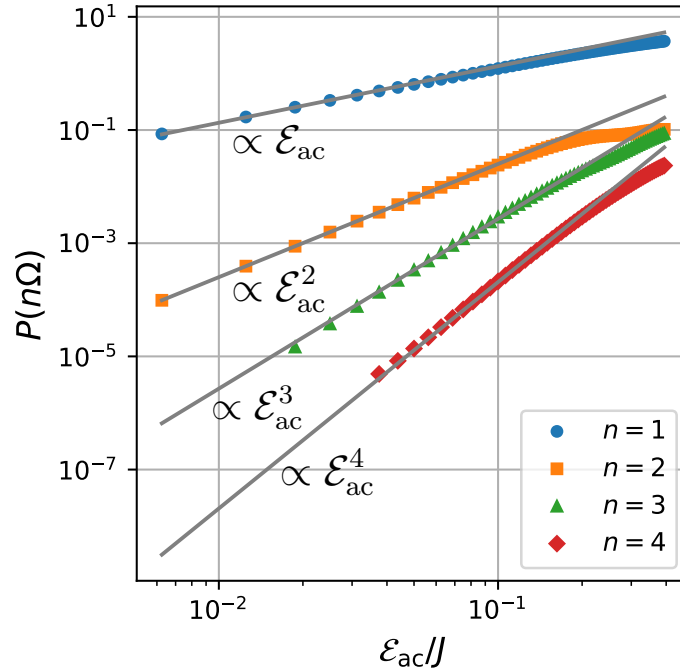


FIG. S18. \mathcal{E}_{ac} dependence of n -th order harmonics of the polarization, $P(n\Omega)$ ($n = 1, 2, 3, 4$), and their fitting lines ($P(n\Omega) \propto \mathcal{E}_{\text{ac}}^n$) in the ferromagnetic ($J > 0$) Kitaev model with $\mathcal{E}_{\text{dc}} = 0.1J$ and $\kappa = 0$ under THz laser pulse of frequency $\Omega = 2.0J$. Due to the small dc electric field of $\mathcal{E}_{\text{dc}} = 0.1J$, the even-order harmonics appear. The relaxation rate is set to be $\gamma = 0.1J$.

Next, we discuss the laser intensity that is necessary for the experiment. Figures S19(a) and S19(b) respectively show the laser-intensity dependence of the ratio $R_n(\Omega) = I(n\Omega)/I(\Omega)$ at zero magnetic field $\kappa = 0$ and at a finite field $\kappa = 0.2|J|$. As we mentioned in the main text, the peak height of the fermion DoS $\mathcal{D}(\Omega)$ increases when κ is applied to the system. Therefore, for the system with $\kappa = 0.2|J|$, the required laser intensity is expected to become smaller than that for the case of $\kappa = 0$. Comparing Figs. S19(a) and S19(b), we find that the ratio $R_{2,3,4}(\Omega)$ become larger when κ is introduced in the system.

To estimate the quantitative value of the required laser intensity, we consider the antiferromagnetic Kitaev magnet with $|J|/k_B = 10$ K and $\mathcal{E}_{\text{dc}} = 0.1J$. In addition, we assume that the strength of the ME coupling is the same as that of the standard Zeeman interaction: $\mathcal{E}_{\text{ac}} = \eta_{\text{ms}} E_{\text{ac}} = g_0 \mu_B E_{\text{ac}}/c$ (c is the speed of light). Under these conditions, one can quantitatively calculate the required laser intensity. From the panel (a), we see that $E_{\text{ac}} = 2.6$ MV/cm at 0.5 THz is necessary for $R_2(\Omega) \gtrsim 10^{-2}$, and $E_{\text{ac}} = 0.9$ MV/cm for $R_2(\Omega) \gtrsim 10^{-3}$ in the Kitaev model with $\kappa = 0$. On the other hand, Fig. S19(b) shows that in the case of $\kappa = 0.2|J|$, the required ac field E_{ac} is estimated as $E_{\text{ac}} = 0.7$ MV/cm at 0.42 THz for $R_2(\Omega) \gtrsim 10^{-2}$, and $E_{\text{ac}} = 0.2$ MV/cm for $R_2(\Omega) \gtrsim 10^{-3}$ (see Table S1). From these results, we can

conclude that low-order harmonic generation in Kitaev magnets can be observed with current THz laser technology.

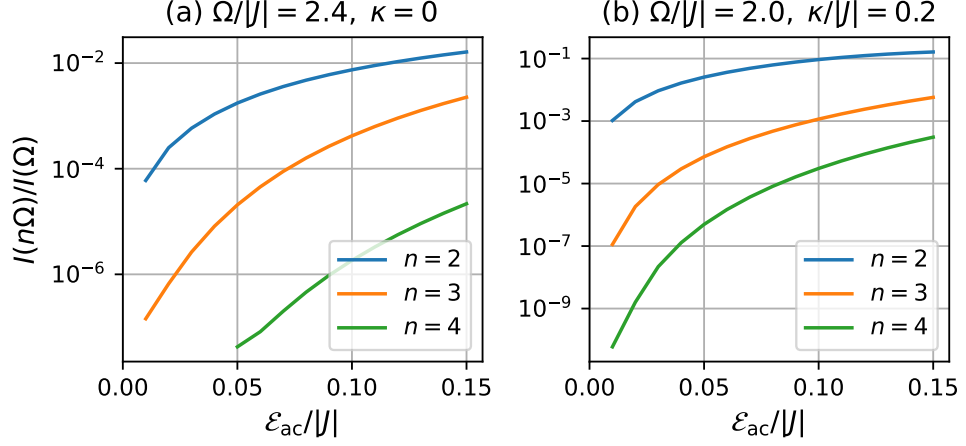


FIG. S19. \mathcal{E}_{ac} dependence of the intensity rate $I(n\Omega)/I(\Omega)$ ($n = 1, 2, 3, 4$) in the antiferromagnetic ($J < 0$) Kitaev models driven by laser pulse of (a) $\Omega = 2.4|J|$ at $\kappa = 0$ and (b) $\Omega = 2.0|J|$ at $\kappa = 0.2|J|$. Other parameters are set to be $\mathcal{E}_{dc} = 0.1|J|$ and $\gamma = 0.1|J|$.

TABLE S1. Required laser intensity for experimental observation of SHG.

Laser-frequency [$f = \Omega/(2\pi)$]	$R_2(\Omega) \gtrsim 10^{-2}$	$R_2(\Omega) \gtrsim 10^{-3}$
0.5 THz	2.6 MV/cm	0.9 MV/cm
0.42 THz ($\kappa = 0.2 J $)	0.7 MV/cm	0.2 MV/cm